Molecules with ALMA at Planet-forming Scales (MAPS). IX. Distribution and Properties of the Large Organic Molecules HC3N, CH3CN, and c-C3H2

John D. Ilee, Catherine Walsh, Alice S. Booth, Yuri Aikawa, Sean M. Andrews, Jaehan Bae, Edwin A. Bergin, Jennifer B. Bergner, Arthur D. Bosman, Gianni Cataldi, et al.

To cite this version:

John D. Ilee, Catherine Walsh, Alice S. Booth, Yuri Aikawa, Sean M. Andrews, et al.. Molecules with ALMA at Planet-forming Scales (MAPS). IX. Distribution and Properties of the Large Organic Molecules HC3N, CH3CN, and c-C3H2. The Astrophysical Journal Supplement Series, 2021, 257, ⟨10.3847/1538-4365/ac1441⟩. ⟨insu-03672372⟩

HAL Id: insu-03672372
https://insu.hal.science/insu-03672372v1

Submitted on 19 Sep 2025

The Astrophysical Journal Supplement Series, 257:9 (20pp), 2021 November https://doi.org/10.3847/1538-4365/ac1441

Molecules with ALMA at Planet-forming Scales (MAPS). IX. Distribution and Properties of the Large Organic Molecules HC_3N, CH_3CN, and c-C_3H_2

John D. Ilee[1], Catherine Walsh[1], Alice S. Booth[1,2], Yuri Aikawa[3], Sean M. Andrews[4], Jaehan Bae[5,6,23], Edwin A. Bergin[7], Jennifer B. Bergner[8,23], Arthur D. Bosman[7], Gianni Cataldi[3,9], L. Ilsedore Cleeves[10], Ian Czekala[11,12,13,14,15,23], Viviana V. Guzmán[16], Jane Huang[4,7,23], Charles J. Law[4], Romane Le Gal[4,17,18,19], Ryan A. Loomis[20], François Ménard[17], Hideko Nomura[9], Karin I. Öberg[4], Chunhua Qi[4], Kamber R. Schwarz[21,23], Richard Teague[4], Takashi Tsukagoshi[9], David J. Wilner[4], Yoshihide Yamato[3], and Ke Zhang[7,22,24]

[1] School of Physics and Astronomy, University of Leeds, Leeds, LS2 9JT, UK; j.d.ilee@leeds.ac.uk
[2] Leiden Observatory, Leiden University, 2300 RA Leiden, The Netherlands
[3] Department of Astronomy, Graduate School of Science, The University of Tokyo, Tokyo 113-0033, Japan
[4] Center for Astrophysics | Harvard & Smithsonian, 60 Garden St., Cambridge, MA 02138, USA
[5] Earth and Planets Laboratory, Carnegie Institution for Science, 5241 Broad Branch Road NW, Washington, DC 20015, USA
[6] Department of Astronomy, University of Florida, Gainesville, FL 32611, USA
[7] Department of Astronomy, University of Michigan, 323 West Hall, 1085 S. University Ave., Ann Arbor, MI 48109, USA
[8] University of Chicago Department of the Geophysical Sciences, Chicago, IL 60637, USA
[9] National Astronomical Observatory of Japan, 2-21-1 Osawa, Mitaka, Tokyo 181-8588, Japan
[10] Department of Astronomy, University of Virginia, Charlottesville, VA 22904, USA
[11] Department of Astronomy & Astrophysics, 525 Davey Laboratory, The Pennsylvania State University, University Park, PA 16802, USA
[12] Center for Exoplanets & Habitable Worlds, 525 Davey Laboratory, The Pennsylvania State University, University Park, PA 16802, USA
[13] Center for Astrostatistics, 525 Davey Laboratory, The Pennsylvania State University, University Park, PA 16802, USA
[14] Institute for Computational & Data Sciences, The Pennsylvania State University, University Park, PA 16802, USA
[15] Department of Astronomy, 501 Campbell Hall, University of California, Berkeley, CA 94720-3411, USA
[16] Instituto de Astrofísica, Pontificia Universidad Católica de Chile, Av. Vicuña Mackenna 4860, 7820436 Macul, Santiago, Chile
[17] Univ. Grenoble Alpes, CNRS, IPAG, F-38000 Grenoble, France
[18] IRAP, Université de Toulouse, CNRS, CNES, UT3, 31400 Toulouse, France
[19] IRAM, 300 rue de la piscine, F-38406 Saint-Martin d'Hères, France
[20] National Radio Astronomy Observatory, 520 Edgemont Rd., Charlottesville, VA 22903, USA
[21] Lunar and Planetary Laboratory, University of Arizona, 1629 E. University Blvd., Tucson, AZ 85721, USA
[22] Department of Astronomy, University of Wisconsin–Madison, 475 N. Charter St., Madison, WI 53706, USA

Received 2021 February 15; revised 2021 May 20; accepted 2021 June 9; published 2021 November 3

Abstract

The precursors to larger, biologically relevant molecules are detected throughout interstellar space, but determining the presence and properties of these molecules during planet formation requires observations of protoplanetary disks at high angular resolution and sensitivity. Here, we present $0\farcs3$ observations of HC_3N, CH_3CN, and c-C_3H_2 in five protoplanetary disks observed as part of the Molecules with ALMA at Planet-forming Scales (MAPS) Large Program. We robustly detect all molecules in four of the disks (GM Aur, AS 209, HD 163296, and MWC 480) with tentative detections of c-C_3H_2 and CH_3CN in IM Lup. We observe a range of morphologies—central peaks, single or double rings—with no clear correlation in morphology between molecule or disk. Emission is generally compact and on scales comparable with the millimeter dust continuum. We perform both disk-integrated and radially resolved rotational diagram analysis to derive column densities and rotational temperatures. The latter reveals 5–10 times more column density in the inner 50–100 au of the disks when compared with the disk-integrated analysis. We demonstrate that CH_3CN originates from lower relative heights in the disks when compared with HC_3N, in some cases directly tracing the disk midplane. Finally, we find good agreement between the ratio of small to large nitriles in the outer disks and comets. Our results indicate that the protoplanetary disks studied here are host to significant reservoirs of large organic molecules, and that this planet- and comet-building material can be chemically similar to that in our own solar system. This paper is part of the MAPS special issue of the Astrophysical Journal Supplement.

Unified Astronomy Thesaurus concepts: Protoplanetary disks (1300); Astrochemistry (75); Interstellar molecules (849); Planet formation (1241)

1. Introduction

Protoplanetary disks host the basic ingredients for planet formation. The abundance and spatial distribution of organic molecules are of particular importance because the most complex of these—the so-called complex organic molecules (COMs)—are the precursors of larger, prebiotic molecules (see, e.g., Herbst & van Dishoeck 2009). These molecules are the vital bridges between the relatively simple molecules that are abundant in circumstellar environments, e.g., CO, and those important for life, such as amino acids. We know that the surface of the young Earth was seeded with organic material via impacts from planetesimals (comets and asteroids) that formed within the disk around the young Sun (see Altwegg et al. 2019). However, it remains unclear whether or not a complex organic reservoir is present in all protoplanetary disks, thus determining their propensity for developing life-friendly environments.

---

[23] NASA Hubble Fellowship Program Sagan Fellow.
[24] NASA Hubble Fellow.

The study of the chemical content of protoplanetary disks began during the advent of (sub)millimeter astronomy that enabled the detection of rotational transitions of small molecules such as CO, HCO^+, CN, CS, C_2H, HCN, HNC, and H_2CO (e.g., Dutrey et al. 1997; Kastner et al. 1997; van Zadelhoff et al. 2001; Aikawa et al. 2003; Thi et al. 2004; Öberg et al. 2010). In these pioneering studies, it was realized that the gas-phase abundances of these species in protoplanetary disks were orders of magnitude lower than those in nearby dark clouds. The prevailing explanation is that disks have a cold, dense midplane where most species are frozen out as ices on dust grain surfaces, and a surface layer where dissociation and ionization dominates. Gas-phase molecules are confined to a warm molecular layer between these two regions (Aikawa et al. 2002). Models suggest that larger molecules can be efficiently formed within the ices on dust grains (e.g., Walsh et al. 2014), and that processes such as nonthermal desorption are required to release these strongly bound molecules into the gas phase. Thus, the detection of emission from such species provides insight into the composition and distribution of the organic ice reservoir.

The younger phases ($\lesssim$1 Myr) of both low- and high-mass star formation host organic-rich reservoirs (for reviews, see Herbst & van Dishoeck 2009; Caselli & Ceccarelli 2012; Jorgensen et al. 2020), but it remains unclear what degree of this organic-rich material is inherited by the protoplanetary disk (e.g., Drozdovskaya et al. 2016, 2019; Bianchi et al. 2019). The unique chemical structure of protoplanetary disks and their small angular size presents challenges when attempting to detect rotational line emission from larger organic molecules. Because the bulk of the mass of protoplanetary disks has a temperature less than $\sim$100 K, most large organics are hosted on ice mantles, significantly reducing the gas-phase abundances. In addition, the larger the molecule, the more complex the spectrum, and the larger the partition function, leading to (in general) significantly weaker emission for individual transitions (Herbst & van Dishoeck 2009). Hence, it has only been very recently that organic molecules with more than four atoms have been successfully detected in protoplanetary disks, and this has been facilitated by the availability of very sensitive, high-angular-resolution observations.

Searches facilitated by interferometers have revealed the prevalence of larger hydrocarbons and complex nitriles in protoplanetary disks. Chapillon et al. (2012), Qi et al. (2013), and Öberg et al. (2015) report the first detections of gas-phase HC_3N (cyanoacetylene), c-C_3H_2 (cyclopropanylidene), and CH_3CN (methyl cyanide) in protoplanetary disks, respectively. Follow-up studies and surveys, facilitated by the Atacama Large Millimeter/submillimeter Array (ALMA), have confirmed the relative ubiquity of these molecules in several nearby well-studied protoplanetary disks (Bergin et al. 2016; Bergner et al. 2018; Kastner et al. 2018; Loomis et al. 2020; Facchini et al. 2021). Their prevalence appears to be connected to an enhanced ratio of elemental carbon relative to elemental oxygen in the disk atmosphere, caused by physical and chemical processing of oxygen-rich ices that effectively removes oxygen from the gas phase (e.g., Kama et al. 2016; Du et al. 2017). On the other hand, oxygen-bearing COMs have remained elusive (Carney et al. 2019). Until recently, CH_3OH and HCOOH had only been detected in the closest protoplanetary disk, TW Hya (Walsh et al. 2016; Favre et al. 2018). Further detections of CH_3OH are now beginning to emerge, but these have so far been confined to young, warm disks (van't Hoff et al. 2018; Lee et al. 2019; Podio et al. 2020) or those with irradiated cavities (Booth et al. 2021). Nonetheless, models have shown that a combination of both gas-phase chemistry and ice-mantle chemistry is needed to explain the abundances of both the complex nitriles and O-bearing organics detected thus far (Loomis et al. 2018a; Le Gal et al. 2019).

In this paper, we report high-angular-resolution ($0\farcs3$) observations of multiple transitions of HC_3N, c-C_3H_2, and CH_3CN toward five nearby protoplanetary disks with ALMA (IM Lup, GM Aur, AS 209, HD 163296, and MWC 480). These data were collected as part of the Molecules with ALMA at Planet-forming Scales (MAPS) Large Program, which has the overarching aim of elucidating the chemistry of planet formation (see Öberg et al. 2021 for further details), and the paper is structured as follows. In Section 2, we outline our methods for detecting, imaging, and analyzing the line emission from each of the target disks. In Section 3, we report images of the line emission, present azimuthally averaged radial profiles of the emission, and use these data to determine both disk-averaged and radially resolved column densities and rotational temperatures (where data quality allows). We compare the obtained molecular distributions and rotational temperatures with those available in the literature. In Section 4, we discuss the trends present in our sample, and compare our retrieved parameters with available model results in order to constrain the chemical origin of these larger hydrocarbons and nitriles. We also compare the radial emission profiles of each molecule with the millimeter dust emission of each disk, and discuss implications of the dust sculpting on the resulting molecular distributions and emission patterns. Finally, we present a future outlook for studies of complex organic molecules in protoplanetary disks.

2. Methods

2.1. Overview of Observations

The data presented here were collected as part of the ALMA Large Program MAPS[25] (project ID 2018.1.01055.L, co-PIs, K. I. Öberg, Y. Aikawa, E. A. Bergin, V. V. Guzmán, and C. Walsh). Full details of the scientific scope and targets of the program are provided in Öberg et al. (2021). Hence, we provide only a brief overview here and limit our description to information pertinent to the scope of this work.

MAPS targeted five protoplanetary disks—IM Lup, GM Aur, AS 209, HD 163296, and MWC 480—using four spectral settings: two in Band 3 and two in Band 6. Together these settings covered 15 transitions of the large organic molecules HC_3N, CH_3CN, and c-C_3H_2 (see Figure 1). Observations using two antenna configurations (compact and extended) were used to recover both large- and small-scale emission from the disks. Standard calibration routines were initially performed by ALMA staff, supplemented by additional self-calibration to improve the signal-to-noise ratio (see Öberg et al. 2021 for full details).

2.2. Matched Filtering

Several of our target lines are predicted to be relatively weak; hence, we initially processed the measurement sets of the line-containing spectral windows using a matched filter as described in Loomis et al. (2018b) (see Figure 2). Several Keplerian filters were attempted with varying radial extents, from the full spatial extent of the ^{12}CO emission, down to very compact filters matched to the emitting radius seen in test images of the target lines. We used the matched filtering response σ_f to define two classes of line detection: tentative

---

[25] http://www.alma-maps.info

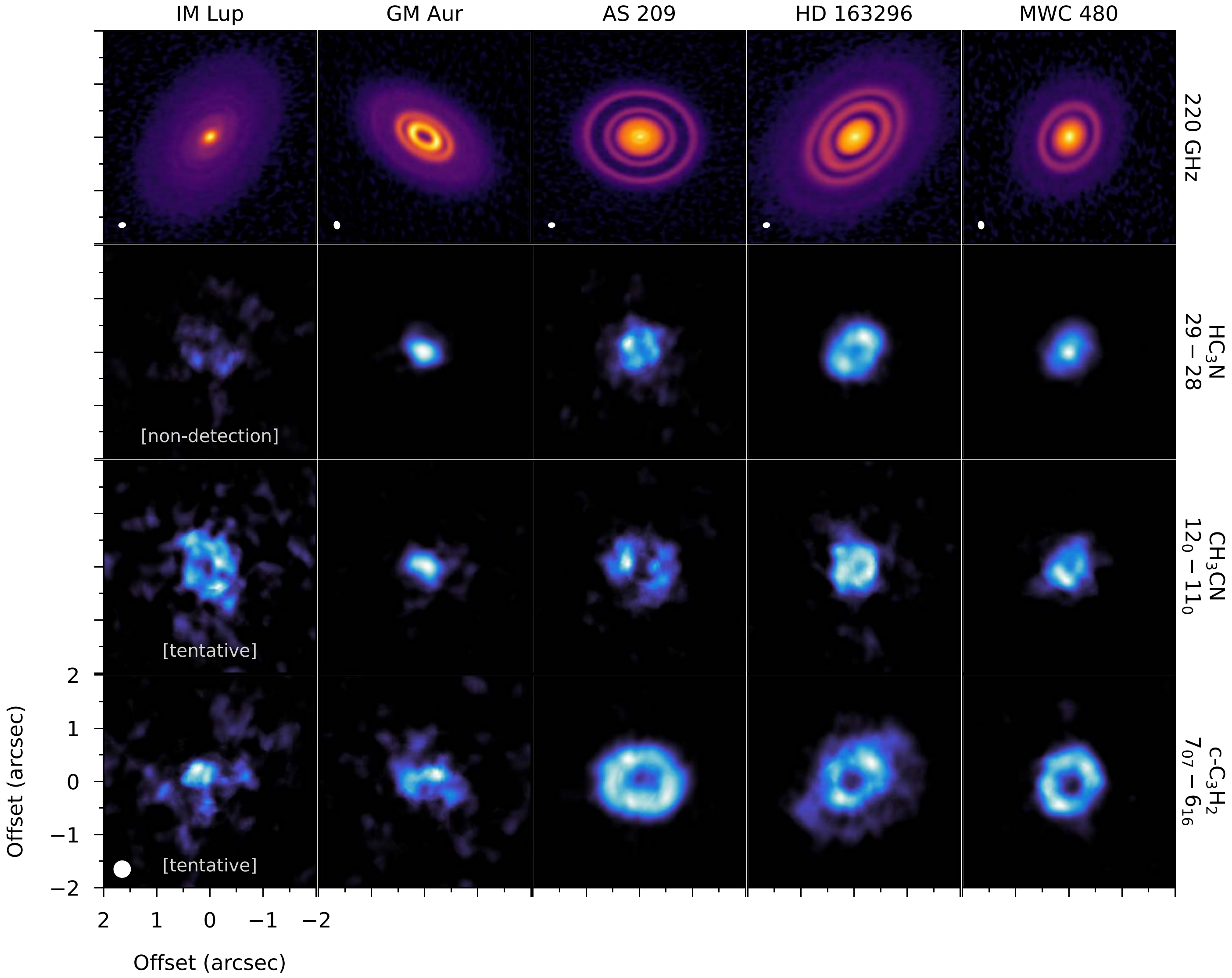

Figure 1. Continuum images at 220 GHz (top) shown alongside integrated intensity (zeroth moment) maps for the brightest transitions of HC_3N, CH_3CN, and c-C_3H_2 in our target disks (bottom). Panels are normalized with continuum and integrated intensity images displayed with power-law and linear stretches, respectively. Beams are shown as a filled ellipse (which is identical for all integrated intensity maps). See Appendix A for a gallery of all transitions with intensity scales, and Sierra et al. (2021) for further information on the continuum images.

(where $3 < \sigma_f < 5$) and robust (where $\sigma_f > 5$). This ensured our criteria for detection were not influenced by our choice of imaging parameters. We further discuss the results of the matched filtering in Section 3.1.

2.3. Imaging

Imaging was performed using the `tclean` task available in `CASA` version 6 (McMullin et al. 2007). During cleaning, Keplerian masks were created based on the known geometry of the disks to select regions in position–position–velocity space with emission. The residual scaling technique of Jorsater & van Moorsel (1995) was applied to the final image cubes to mitigate artifacts introduced by the combination of data from multiple antenna configurations. Detailed explanations of these steps are provided in Czekala et al. (2021).

In this work, we make use of the fiducial MAPS imaging products. Given the aforementioned weak nature of many of our targeted lines, coupled with the fact that we compare observations across ALMA Bands 3 and 6, all data presented in this paper utilize images with circularized beams of size $\sim 0\farcs3$, obtained by applying a *uv* taper during imaging (see Section 6.2 of Czekala et al. 2021). This was found to provide the optimal combination of angular resolution and sensitivity for our analysis. All image cubes were post-processed in a homogeneous manner through our dedicated pipeline to produce integrated intensity maps (zeroth moment; see Figure 1 and Appendix A) and azimuthally averaged radial emission profiles (see Section 3.3 and Law et al. 2021a, for further details).

2.4. Shifting and Stacking

In order to robustly recover emission in the image plane from the weakest transitions, we utilize the line shifting and stacking technique available within the `GoFish` package, making use of the `integrated_spectrum()` function (Teague 2019). This approach exploits the known geometry and velocity structure of the disk to deproject the rotation profile and combine Doppler shifted emission to a common centroid velocity reference frame. This results in a single disk-integrated

Table 1
Peak Matched Filter Response (σ_f) and Disk-integrated Fluxes ($S_\nu\,\Delta v$) for Each Transition and Disk

Transition	Frequency (GHz)	IM Lup		GM Aur		AS 209		HD 163296		MWC 480	
		σ_f	$S_\nu\,\Delta v$ (mJy km s^{-1})	σ_f	$S_\nu\,\Delta v$ (mJy km s^{-1})	σ_f	$S_\nu\,\Delta v$ (mJy km s^{-1})	σ_f	$S_\nu\,\Delta v$ (mJy km s^{-1})	σ_f	$S_\nu\,\Delta v$ (mJy km s^{-1})
HC_3N											
11–10	100.0763920	<3	<11.5	14.7	31.3 ± 5.5	27.6	118.0 ± 6.6	32.8	128.8 ± 5.6	26.9	74.1 ± 5.8
29–28	263.7923080	<3	<4.3	11.1	87.7 ± 2.3	9.9	38.5 ± 2.3	24.4	196.9 ± 3.0	19.0	124.2 ± 3.1
CH_3CN											
6_5–5_5	110.3303454	<3	<3.9	<3	<2.9	<3	<5.3	<3	<2.7	<3	<7.6
6_4–5_4	110.3494707	<3	<3.6	<3	<2.6	<3	<5.1	<3	<2.5	<3	<8.2
6_3–5_3	110.3643540	<3	<3.6	<3	<2.7	<3	<5.4	<3	<2.7	<3	<8.8
6_2–5_2	110.3749894	<3	<3.5	3.1	1.1 ± 0.9	<3	<5.7	<3	<2.8	<3	<9.2
6_1–5_1[a]	110.3813723	<3	<3.6	3.4	5.3 ± 1.0	5.5	12.1 ± 1.8	4.1	5.6 ± 0.9	6.7	16.6 ± 2.8
6_0–5_0[a]	110.3835002	<3	<3.6	3.2	3.0 ± 0.9	6.1	8.6 ± 1.7	3.0	7.8 ± 0.9	7.7	8.9 ± 2.7
12_3–11_3	220.7090174	<3	<3.7	4.8	5.9 ± 0.3	<3	<4.3	3.2	8.2 ± 0.8	9.1	22.8 ± 1.3
12_2–11_2	220.7302611	<3	<3.5	7.9	9.3 ± 0.4	<3	<4.1	6.5	12.5 ± 0.8	8.0	26.1 ± 1.3
12_1–11_1[a]	220.7430111	3.7	12.1 ± 1.2	12.6	12.8 ± 0.4	7.4	15.3 ± 1.5	8.2	22.8 ± 0.9	14.1	31.4 ± 1.4
12_0–11_0[a]	220.7472617	<3	<3.6	10.9	14.2 ± 0.4	9.2	24.3 ± 1.4	7.9	22.3 ± 0.8	16.4	44.3 ± 1.2
c-C_3H_2											
7_{07}–6_{16}[b]	251.3143670	4.2	6.1 ± 1.4	8.4	27.4 ± 1.6	52.2	228.1 ± 5.8	51.1	146.8 ± 2.8	25.0	119.9 ± 3.2
6_{15}–5_{24}	251.5087085	<3	<4.4	<3	<4.7	11.2	43.9 ± 2.4	9.8	28.4 ± 1.9	5.4	20.9 ± 2.7
6_{25}–5_{14}	251.5273110	<3	<4.3	7.2	11.5 ± 1.7	31.9	133.3 ± 4.0	28.4	91.4 ± 2.5	14.8	72.2 ± 2.7

Notes.
[a] CH_3CN $K = 0$ and $K = 1$ are blended; fluxes are measured following the method outlined in Section 2.4.
[b] Includes blended para transition (7_{17}–6_{06}) at the same frequency; see Section 3.4.

spectrum for each transition that we use to measure a disk-integrated line flux (or a corresponding upper limit in the case of nondetections). Velocity ranges for integration are chosen by eye for each transition to include all positive emission in the main core of the line. Uncertainties are calculated on a per channel basis, taking into account decorrelation along the spectral axis (see also Yen et al. 2016). Figure 3 shows examples of the stacking technique for several transitions in MWC 480, and Table 1 reports these measurements for all transitions and targets.

We note that the measurement of line flux for the CH_3CN $K = 0$ and $K = 1$ transitions is complicated by their separation of only $\sim$6 km s^{-1}, leading to significant blending at higher velocities. We attempted to mitigate this by use of a sufficiently tight Keplerian mask, but contamination still occurred (as can be seen in Figure 3). Since these lines are expected to produce symmetric profiles, we therefore adopt the approach shown in Figure 3 for these transitions that involves measuring the line flux from the unblended half of the integrated spectrum and assuming symmetry about the rest velocity of the line in order to recover the full line flux.

2.5. Rotational Diagrams

We exploit the fact that we have multiple transitions of each molecule to empirically extract both disk-integrated and radial-dependent column densities, N_T, and rotational temperatures, $T_{\rm rot}$, wherever possible. Our methodology, which is similar to that presented in Loomis et al. (2018a), can be described as follows. Under the assumption of optically thin emission, the surface brightness of line emission I_ν is related to the column density of molecules in the upper level of each transition $N_u^{\rm thin}$ via

$$I_\nu = \frac{A_{\rm ul} N_u^{\rm thin} hc}{4\pi \Delta v}, \tag{1}$$

in which $A_{\rm ul}$ is the Einstein A coefficient and Δv is the intrinsic line width (see, e.g., Goldsmith & Langer 1999). In the case of disk-averaged emission, $I_\nu = S_\nu/\Omega$, where S_ν is the flux density and Ω is the solid angle subtended by the emission, calculated from the radial extent of each line. Substituting for I_ν and inverting this relation gives

$$N_u^{\rm thin} = \frac{4\pi S_\nu \Delta v}{A_{\rm ul}\,\Omega hc}, \tag{2}$$

where $S_\nu \Delta v$ is the integrated flux density reported for each of the transitions in Table 1.

This can then be related to the total column density of the emission through the Boltzmann distribution,

$$\frac{N_u}{g_u} = \frac{N_T}{Q(T_{\rm rot})} e^{-E_u/k_B T_{\rm rot}}, \tag{3}$$

where g_u and E_u are the degeneracy and energy of the upper level, respectively (see Appendix B), and $Q(T_{\rm rot})$ is the partition function at the rotational temperature (linearly interpolated in log-space from calculated values tabulated in the Cologne Database for Molecular Spectroscopy (CDMS); see Müller et al. 2005). Taking the logarithm of Equation (3) yields

$$\ln \frac{N_u^{\rm thin}}{g_u} = \ln N_T - \ln Q(T_{\rm rot}) - \frac{E_u}{k_B T_{\rm rot}}, \tag{4}$$

which can form the basis of a linear least-squares regression that derives the rotational temperature, $T_{\rm rot}$, and total column density, N_T, from the best-fitting slope and intercept, respectively.

In the case that τ is not negligible, an optical depth correction factor, C_τ, must be applied such that the true level populations become

$$N_u = N_u^{\rm thin} C_\tau, \quad (5)$$

where $C_\tau = \tau/(1 - e^{-\tau})$ and Equation (4) can then be expressed as

$$\ln \frac{N_u^{\rm thin}}{g_u} + \ln C_\tau = \ln N_T - \ln Q(T_{\rm rot}) - \frac{E_u}{k_B T_{\rm rot}}. \quad (6)$$

The optical depth of individual transitions can be related back to the upper state level populations via

$$\tau_{\rm ul} = \frac{A_{\rm ul} c^3}{8\pi \nu^3 \Delta v} N_u (e^{h\nu/k_B T_{\rm rot}} - 1), \quad (7)$$

which implies that C_τ can be written as a function of N_u and substituted into Equation (6) in order to construct a likelihood function $\mathcal{L}$(data, N_T, $T_{\rm rot}$) to be used for χ^2 minimization. We use the Markov Chain Monte Carlo (MCMC) code `emcee` (Foreman-Mackey et al. 2013) to fit the observed data using this likelihood function, generating posterior probability distributions that describe the range of possible values of both N_T and $T_{\rm rot}$. Best-fitting values and their uncertainties are chosen from the median and 16th–84th percentile of these posterior distributions, respectively. We assume uniform priors spanning ranges of $10^8 < N_T < 10^{15}$ cm^{-2} and $1 < T_{\rm rot} < 150$ K, respectively, which encompasses the typical values expected for these molecules in disks (see, e.g., Bergner et al. 2018).

The intrinsic line width, Δv, can be described as a combination of thermal and turbulent broadening such that

$$\Delta v = 2\sqrt{\ln 2}\sqrt{\frac{2 k_B T_{\rm ex}}{m_X} + t_0^2 \frac{k_B T_{\rm ex}}{\mu m_{\rm H}}}, \quad (8)$$

where m_X and $m_{\rm H}$ are the masses of the molecule and hydrogen, respectively, $\mu = 2.37$ is the assumed mean molecular weight, and $t_0 \sim 0.01$ is the assumed contribution to the line width from turbulence (expected to be small in the line-emitting region of protoplanetary disks; see, e.g., Flaherty et al. 2015). Since Δv is a function of temperature, we iterate the fitting procedure assuming $T_{\rm ex} = T_{\rm rot}$ until the resulting best-fitting values for column density and rotational temperature converge, which is usually achieved within $\lesssim$5 iterations.

For the determination of radially resolved quantities, we perform the same procedure as for the disk-integrated analysis but where $S_\nu \Delta v$ is obtained from the radial profiles in annular bins of width $0\farcs075$ (one quarter of a beam) and Ω is the solid angle of each annulus. In these cases, the MCMC fitting procedure is performed independently for each bin, and the results are combined to report values of $N_T(r)$, $T_{\rm rot}(r)$, and $\tau(r)$ for each molecule in each disk.

3. Results

Here, we present the results of the matched filter analysis and the imaging, including the generated zeroth-moment maps and azimuthally averaged radial profiles, along with disk-averaged and radially resolved rotational diagram analysis for each disk.

3.1. Matched Filter Detections

As explained in Section 2, all line-containing spectral windows were analyzed using a matched filter to confirm the detection of each of our targeted species and lines (see Loomis et al. 2018a, for full details). We used a Keplerian filter that was manually varied in radial extent to achieve the highest filter response (σ_f) for each molecule. We found that a 200 au radius filter was optimal for HC_3N and c-C_3H_2, whereas a more compact filter with a radius of 100 au provided the strongest filter response for CH_3CN, indicating the more compact nature of the emission from this species. The results of the matched filter are shown in Figure 2.

We strongly detect ($\sigma_f \gtrsim 10$) both lines of HC_3N in four out of five of our sources, but it is not detected in IM Lup. We also strongly detect ($\sigma_f > 10$) the 7_{07}–6_{16} and 6_{25}–5_{14} transitions of c-C_3H_2 in all disks except IM Lup (where there is only a tentative detection of the 7_{07}–6_{16} transition). The 6_{15}–5_{14} transition of c-C_3H_2 is detected with $\sigma_f > 5$ in three out of five sources (AS 209, HD163296, and MWC 480).

For CH_3CN, we targeted the K-ladder of the $J = 6$–5 transition in Band 3 and the $J = 12$–11 transition in Band 6. In both cases, the $K = 0$ and $K = 1$ lines are blended. These transitions of the 12–11 line of CH_3CN are well detected in all sources except IM Lup, for which there is a tentative detection of the 12_1–11_1 transition only ($\sigma_f \sim 3$). Further, we detect emission also from the 12_2–11_2 transition in GM Aur, HD 163296, and MWC 480. The emission from CH_3CN in Band 3 is significantly weaker. We detect the 6_0–5_0 and 6_1–5_1 lines only in AS 209, HD 163296, and MWC 480. There is a tentative detection ($\sigma_f \sim 3$) of these transitions as well as the 6_2–5_2 transition in GM Aur.

In summary, we have detected at least two transitions of each of our targeted species in all disks except IM Lup. We confirm the previously reported detections of CH_3CN and HC_3N in HD 163296 and MWC 480 by Öberg et al. (2015) and Bergner et al. (2018), and report new detections of these species in GM Aur and AS 209, as well as a tentative detection of CH_3CN in IM Lup. Further, we report new detections of c-C_3H_2 in three sources (GM Aur, AS 209, and MWC 480) and confirm the previous detection in HD 163296 reported by Qi et al. (2013).

3.2. Integrated Intensity Maps

Figure 1 presents integrated intensity (zeroth moment) maps for the brightest transitions of HC_3N, CH_3CN, and c-C_3H_2 in our target disks (the full gallery of all transitions in all disks is shown in Appendix A).

The c-C_3H_2 emission has a clear ring-like morphology in AS 209, HD 163296, and MWC 480 for both transitions, potentially indicative of an association with the outer dust rings apparent in the continuum images (see Figure 1). The zeroth-moment maps show that emission from this species is weaker in GM Aur and only very tentatively present in IM Lup (confirming the matched filter analysis; see Figure 2). HC_3N also presents a ring-like morphology in both the $J = 11$–10 and 29–28 transitions toward AS 209 and HD 163296, while only the $J = 11$–10 transition appears ring-like toward MWC 480 (with the $J = 29$–28 appearing centrally peaked). GM Aur initially appears to be an outlier with centrally peaked HC_3N emission in both transitions, but we note that a ring-like morphology is also observed toward this source when examining higher-resolution data ($0\farcs15$; see Law et al. 2021a). In most cases, the $J = 11$–10 transition of HC_3N emission is similarly extended to that of c-C_3H_2. However, the higher-energy $J = 29$–28 transition ($E_u = 190$ K) appears more compact in all disks in which it is well detected. For CH_3CN,

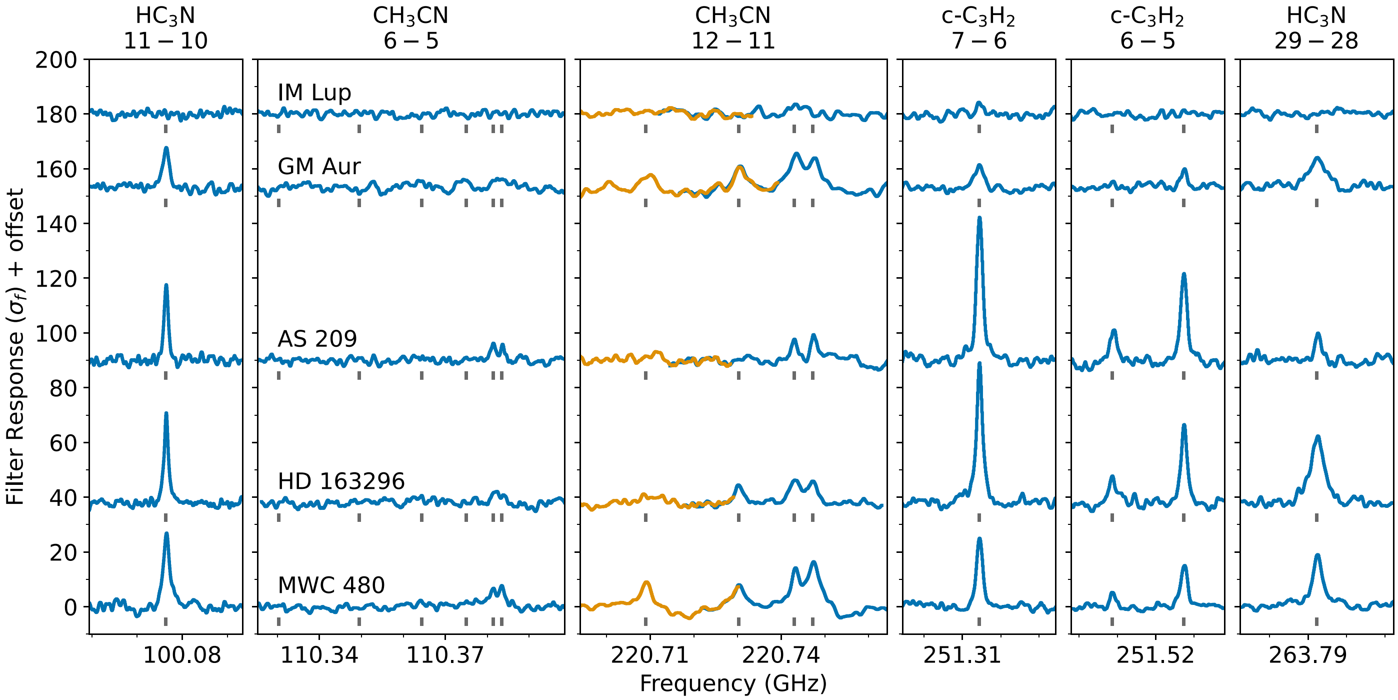

Figure 2. Matched filter response σ_f across the (rest) frequency range each of the targeted transitions (vertically offset for clarity). Multiple spectral windows are shown with different line colors, and vertical dashed lines mark the rest frequencies of transitions.

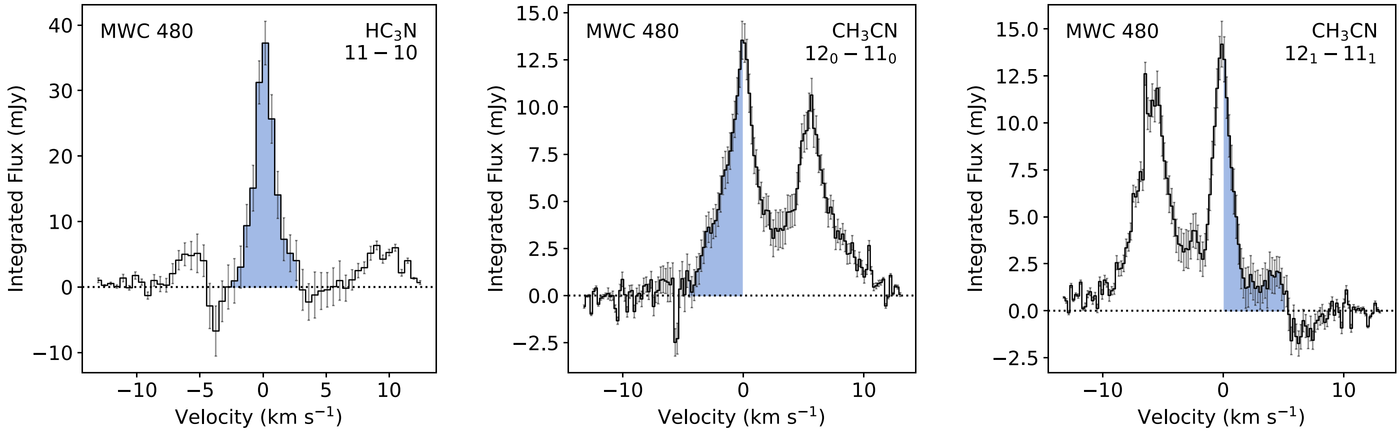

Figure 3. Examples of the spectral shifting and stacking procedure for selected lines in the MWC 480 disk in Band 3 (HC$_3$N 11–10, left) and Band 6 (CH$_3$CN 12–11; middle, right). Uncertainties are shown for each channel, and the shaded region indicates the velocity range across which the line flux was measured (assumed to represent 50% of the total line flux for the blended CH$_3$CN $K = 0$ and $K = 1$ transitions; see Section 2.4).

lines in the $J = 6$–5 ladder are significantly weaker than those in the $J = 12$–11 ladder. In contrast to the emission morphology for *c*-C$_3$H$_2$ and HC$_3$N, CH$_3$CN appears to have a clear ring-like morphology only in AS 209, with a more centrally peaked morphology present in the other sources in which it is well detected (although we note the presence of minor dips of emission in the innermost regions of HD 163296 and MWC 480 on scales comparable to the beam).

3.3. Radial Profiles

Radial profiles are particularly powerful at revealing substructure not immediately apparent in the integrated intensity maps, and allow us to quantify the radial extent of the emission. Figure 4 shows the azimuthally averaged radial profiles of emission (see Law et al. 2021a for details on how these are generated) of all lines detected in four of our sources: AS 209, GM Aur, HD 163296, and MWC 480. IM Lup possessed numerous nondetections, and even those lines that were found were only detected at tentative significance, so we exclude this disk from the subsequent radial analysis.

Figure 4 confirms both the relatively compact nature of emission from this suite of large organic molecules as well as the ringed morphology present in many sources. HC$_3$N exhibits either a ringed morphology (in AS 209 and HD 163296) or a centrally compact morphology (GM Aur and MWC 480). For AS 209, the lower-energy transition ($J = 11$–10; $E_u = 28.8$ K) is stronger than the higher-energy transition ($J = 29$–28; $E_u = 190$ K), by up to a factor of ∼1.5 at their peak positions. For all other sources, the converse is true, with the higher-energy transition between factors of ∼1.5–3 stronger at the peak of emission. In all disks, the HC$_3$N emission extends out only to the outer edge of the millimeter dust disk. For AS 209,

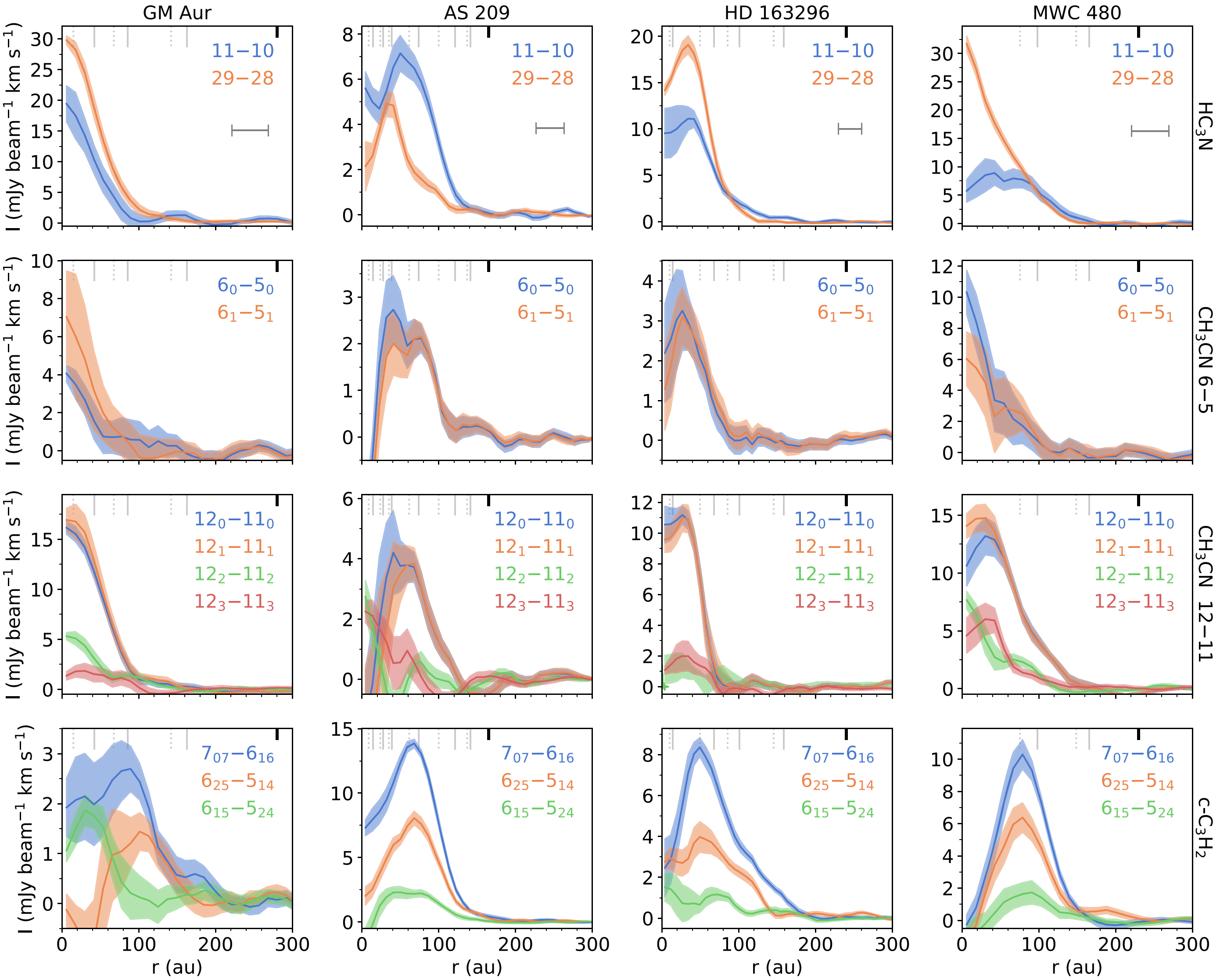

Figure 4. Azimuthally averaged radial emission profiles for HC$_3$N, CH$_3$CN, and *c*-C$_3$H$_2$ in all sources in which the lines are well detected: AS 209, GM Aur, HD 163296, and MWC 480. Locations of continuum rings and gaps are marked with gray vertical lines (solid and dotted, respectively) with the extent of the continuum marked in black (see Law et al. 2021a, their Appendix F). The beam FWHM for each disk is shown in the top panels with a horizontal bar.

the emission from the lower-energy transition peaks at ∼50 au, which lies between the third and forth millimeter dust rings (Guzmán et al. 2018b). Similarly, both transitions of HC$_3$N in HD 163296 peak at ∼40 au, which lies between the first and second millimeter dust rings in the high-resolution Band 6 continuum image (Isella et al. 2018). However, there is a large caveat with regard to this comparison, namely that the synthesized beam of the high-resolution continuum images is significantly smaller than that of the lines (0.″03 versus 0.″3).

The radial profiles for CH$_3$CN are either centrally peaked (GM Aur and HD 163296) or display a broad ring (AS 209 and MWC 480) where the latter peaks at radii between ∼30–50 au depending on transition. In all disks, the emission extent is well within the millimeter dust. In all cases, the 12_0–11_0 and 12_1–11_1 transitions are the strongest (E_u= 68.9 K and 76.0 K, respectively). These two Band 6 transitions are considerably stronger than the equivalent Band 3 transitions (i.e., 6_0–5_0 and 6_1–5_1; E_u= 18.5 K and 25.7 K, respectively) for all disks by factors of 2–3.

Finally, the radial profiles for *c*-C$_3$H$_2$ present a mostly ring-like morphology in all cases. This emission appears to be related to the location of millimeter dust gaps in AS 209, HD 163296, and MWC 480 (at 60 au, 50 au, and 80 au, respectively), in agreement with the analysis of the higher-resolution (0.″15) imaging products (Law et al. 2021a). However, for AS 209 and HD 163296, the *c*-C$_3$H$_2$ emission peaks outside of that for HC$_3$N, highlighting that any correlations between dust continuum and line emission can be different for different molecules. The *c*-C$_3$H$_2$ emission is confined to within the outer edge of millimeter emission, except for GM Aur, where there is weak extended emission. In all cases, the 7_{07}–6_{16} transition is the stronger of the two, although this is mainly reflecting the difference in the Einstein A coefficients for the transitions (see Table 4), as these two transitions have very similar upper energy levels. In summary, there is not a one-to-one relation between line emission from a specific species and dust morphology, nor is there a straightforward correlation between the morphology of emission between different species, except that HC$_3$N and CH$_3$CN

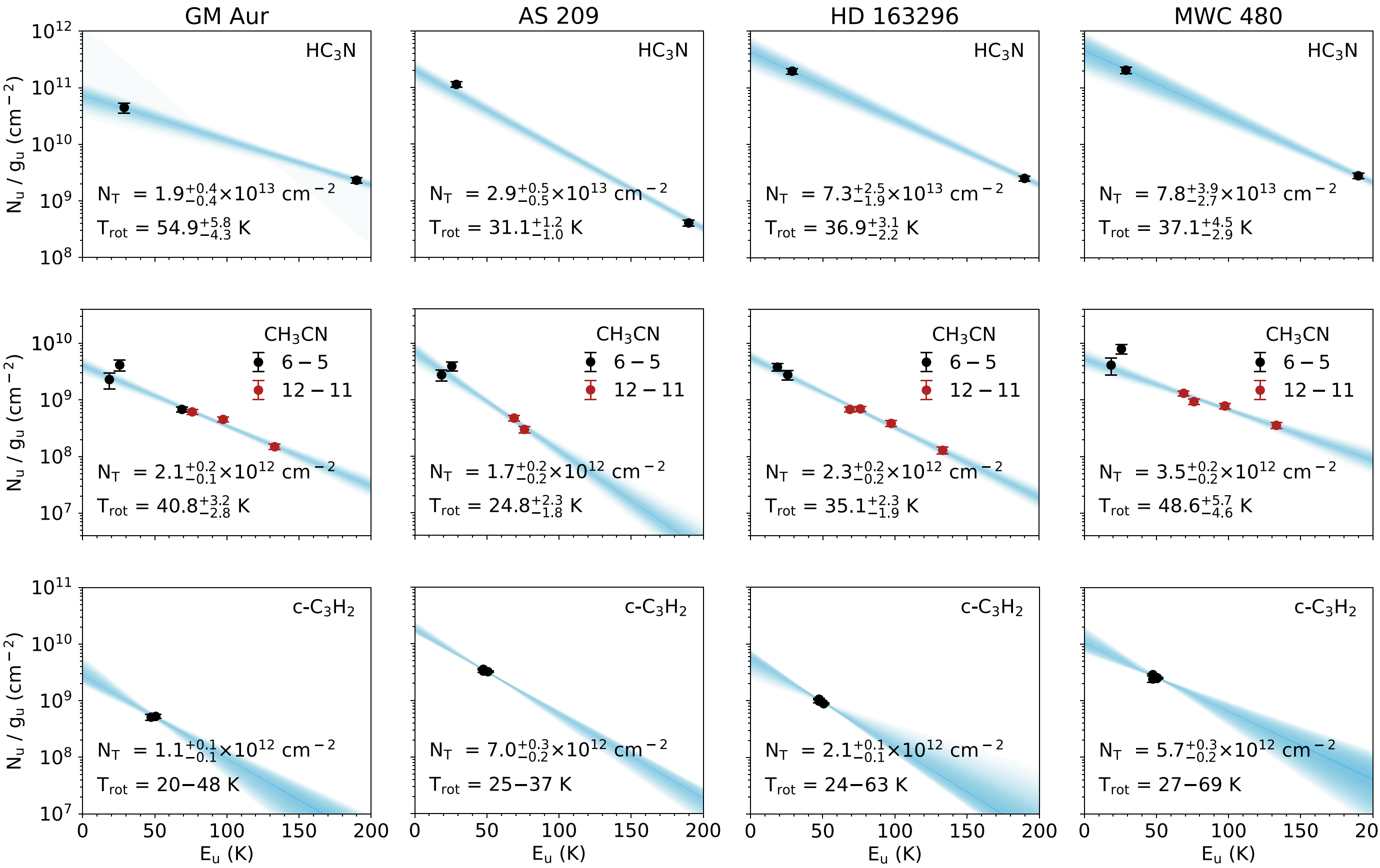

Figure 5. Disk-integrated rotational diagrams for HC_3N (top), CH_3CN (middle), and c-C_3H_2 (bottom) labeled with derived N_T and $T_{\rm rot}$ values and their uncertainties. Random draws from the corresponding posterior probability distribution are shown in blue. Due to the limited range of E_u spanned by our targeted c-C_3H_2 transitions, $T_{\rm rot}$ is restricted during fitting as described in Section 3.4.1.

appear broadly similar across each disk. There are several explanations for the presence of ringed emission in molecular lines in protoplanetary disks (now widely observed; see, e.g., Pegues et al. 2020; Garufi et al. 2021), including a drop in column density in the inner regions due to destructive chemical reactions, an increase in opacity in either dust or lines masking emission from deeper layers in the inner disk regions, or a change in excitation conditions (see, e.g., Facchini et al. 2018; van der Marel et al. 2018; Alarcón et al. 2020). The one constant across the large organic species and disks is that all transitions originate on scales either less than, or comparable to, the extent of the the millimeter dust continuum in each disk.

3.4. Column Densities and Rotational Temperatures

Here, we present the results of the calculations of both the disk-integrated and radially resolved column densities (N_T) and rotational temperatures ($T_{\rm rot}$) using the methods outlined in Section 2.5. As noted in Table 1, our measurements of the c-C_3H_2 7_{07}–6_{16} line are blended with the corresponding para transition (7_{17}–6_{06}) at the same frequency (see Spezzano et al. 2012). For the purposes of the subsequent analysis, we correct the disk-integrated and radially resolved measurements of this line assuming equal contributions from each transition and an ortho-to-para ratio of 3, representative of measurements in other protoplanetary disks (see, e.g., Guzmán et al. 2018a; Terwisscha van Scheltinga et al. 2021; Cleeves et al. 2021).

3.4.1. Disk-integrated Analysis

Figure 5 shows the results of the disk-integrated rotational diagram analysis for the four disks across which multiple transitions of HC_3N, CH_3CN, and c-C_3H_2 are detected. For all analysis in which data from multiple observing epochs and bands are used, we assume an additional 10% error to account for uncertainties in flux calibration. All disk-integrated column densities and rotational temperatures are presented in Table 2.

We note that, for c-C_3H_2, both targeted transitions are very close in upper energy level. This significantly limits the lever arm over which to calculate a gradient and thus rotational temperature. We therefore limit the range of priors for c-C_3H_2 such that $T_{\rm mid,0} < T_{\rm rot} < T_{\rm atm,0}$, where $T_{\rm mid,0}$ and $T_{\rm atm,0}$ are the midplane and atmospheric temperature at a radial distance of 100 au for each disk, derived from fitting multiple CO isotopologues (see Appendix C, Table 5, and Law et al. 2021b).

Where detected, the disk-integrated column of HC_3N ranges from 1.9×10^{13} cm^{-2} for GM Aur to 7.8×10^{13} cm^{-2} for MWC 480. The disk-integrated rotational temperatures are relatively constant across AS 209, HD 163296, and MWC 480 at ∼30–37 K, but somewhat higher in GM Aur at 55 K. It is important to note that the $J = 11$–10 transition in all disks appears to be close to optically thick with $\tau = 0.4$–2.8, which may suggest there is a reservoir of HC_3N in the disks not probed by our observations.

The disk-integrated column of CH_3CN presents a narrow range with all values lying within 1.7–3.5×10^{12} cm^{-2}, though

Table 2
Median Values of Column Density (N_T), Rotational Temperature ($T_{\rm rot}$), and Maximum Optical Depth ($\tau_{\rm max}$) from the Fitting Procedure to the Disk-integrated Rotational Diagrams

	HC_3N			CH_3CN			c-C_3H_2		
	N_T (cm^{-2})	$T_{\rm rot}$ (K)	$\tau_{\rm max}$	N_T (cm^{-2})	$T_{\rm rot}$ (K)	$\tau_{\rm max}$	N_T (cm^{-2})	$T_{\rm rot}$ (K)	$\tau_{\rm max}$
IM Lup	$<5.5 \times 10^{12}$	⋯	⋯	$<6.5 \times 10^{11}$	⋯	⋯	$<7.3 \times 10^{11}$	⋯	⋯
GM Aur	$1.9^{+0.4}_{-0.4} \times 10^{13}$	$54.4^{+5.8}_{-4.3}$	0.40	$2.1^{+0.2}_{-0.1} \times 10^{12}$	$40.8^{+3.2}_{-2.8}$	0.04	$1.1^{+0.1}_{-0.1} \times 10^{12}$	20–48	0.04
AS 209	$2.9^{+0.5}_{-0.5} \times 10^{13}$	$31.1^{+1.2}_{-1.0}$	1.85	$1.7^{+0.2}_{-0.2} \times 10^{12}$	$24.8^{+2.3}_{-1.8}$	0.11	$7.0^{+0.3}_{-0.2} \times 10^{12}$	25–37	0.24
HD 163296	$7.3^{+2.5}_{-1.9} \times 10^{13}$	$36.9^{+3.1}_{-2.2}$	2.62	$2.3^{+0.2}_{-0.2} \times 10^{12}$	$35.1^{+2.3}_{-1.9}$	0.07	$2.1^{+0.1}_{-0.1} \times 10^{12}$	24–63	0.03
MWC 480	$7.8^{+3.9}_{-2.7} \times 10^{13}$	$37.1^{+4.5}_{-2.9}$	2.83	$3.5^{+0.2}_{-0.2} \times 10^{12}$	$48.6^{+5.7}_{-4.6}$	0.06	$5.7^{+0.3}_{-0.2} \times 10^{12}$	27–69	0.14

Note. Uncertainties correspond to the 16th-84th percentile of the posterior probability distribution of the MCMC fitting procedure.

a larger range in rotational temperature is seen for the CH_3CN emission across the disks in the sample with $T_{\rm rot} \sim 25$–49 K. The calculated optical depths indicate that CH_3CN emission is optically thin in all disks (though our radially resolved analysis reveals CH_3CN may be optically thick across some limited regions of the disks; see Section 3.4.2).

For c-C_3H_2, there is around a factor of six spread in the disk-integrated column densities ranging from 1.1×10^{12} cm^{-2} in GM Aur to 7.0×10^{12} cm^{-2} in AS 209. We again note that the rotational temperatures are constrained based on the temperature structure of the disks rather than population diagrams. Based on these assumptions, it appears c-C_3H_2 is optically thin across all disks.

The nondetection of HC_3N and only tentative detections of a single CH_3CN and c-C_3H_2 transition toward IM Lup prevents any determination of well-constrained values for rotational temperature or column density for these molecules. However, by performing the disk-integrated analysis where nondetections provide upper limits, we are able to determine the corresponding upper limit to column density for these molecules in the IM Lup disk (see Table 2). The resulting HC_3N column density of $\lesssim 5.5 \times 10^{12}$ cm^{-2} is a factor of 3–15 times lower than values found in the other disks. Similarly, the upper limit for the column of CH_3CN and c-C_3H_2 in IM Lup are factors of 3–5 and 2–8 times lower than for the other disks, respectively.

3.4.2. Radially Resolved Analysis

The disk-integrated analysis demonstrates interesting similarities and differences across the molecules and sources in our small sample. Since the emission is spatially resolved in most cases, this allows us to also conduct a radially resolved excitation analysis to examine radially dependent variations that cannot be probed by a disk integrated analysis. Figure 6 shows the results of this analysis presenting the radial-dependent rotational temperature, column density, and optical depth profiles for all molecules and sources in which emission is well detected.

For HC_3N, the radial column densities reveal some structure, with a plateau of higher column densities typically reached in the inner ($\lesssim$100 au) region ($\sim 10^{14}$ cm^{-2}) declining monotonically with radius to $\sim 10^{13}$–10^{12} cm^{-2} beyond ~50–100 au. The rotational temperature is also relatively constant across all disks at ~50 K. There is an indication of an increase in rotational temperature within the inner 20–30 au of GM Aur and MWC 480, although derived quantities in these regions may be affected by issues such as beam smearing. In addition, the emission from the $J = 11$–10 transition of HC_3N appears to be optically thick throughout a significant radial region of each disk, sometimes as far out as 130 au. Hence, it is possible that there is a significant reservoir of HC_3N in these regions of these disks to which our observations are not sensitive, and so our radially resolved column densities are likely lower limits in these regions.

For CH_3CN, there are more differences seen between disks in the radially resolved column densities than for HC_3N. This is despite the disk-integrated analysis suggesting very similar disk-integrated columns across all four sources. In general, the radially resolved column densities are between a factor of 5–10 higher than those derived from the disk-integrated analysis. For GM Aur and MWC 480, the column density monotonically decreases with radius from $\sim 5 \times 10^{13}$ cm^{-2} to a few 10^{12} cm^{-2} at approximately 100 au. On the other hand, the column density of CH_3CN in AS 209 and HD 163296 has more of a broad ring-like structure. The rotational temperatures of CH_3CN appear to show a similar radial behavior across all sources, remaining relatively constant at 30–40 K within ~100 au, which is similar to values derived from the disk-integrated analysis. There are hints of a rise to ~80 K in the outer regions of GM Aur and AS 209, but this may be due to a limited signal-to-noise ratio in these regions. There is also a significant rise in rotational temperature in the inner region of AS 209 to ~80 K, as expected based on the weak $K = 0$ and $K = 1$ lines across this region (although we note that the uncertainties here are large). Our analysis also reveals that the CH_3CN Band 3 lines, in particular the 6_0–5_0 and 6_1–5_1 transitions, approach optical depths of 1 or higher out to 100 au in three of the disks (AS 209, HD 163296, and MWC 480) and in the inner regions ($\lesssim$20 au) of GM Aur. This indicates that, similarly to HC_3N, our observations may not be sensitive to the bulk of the CH_3CN emitting material.

For the radially resolved analysis of c-C_3H_2, we are again limited in our calculation of a rotational temperature by the small difference in upper energy level of the targeted transitions. We therefore fix the rotational temperature to the one-dimensional power-law profile, $T(r) = T_{100} \times \left(\frac{r}{100\ {\rm au}}\right)^{-q}$, fitted to the ^{13}CO $J = 2$–1 brightness temperature for each disk (see Table 5 in Appendix C and Law et al. 2021b), that we extrapolate to all radii covered by our c-C_3H_2 emission. In all cases, the emission is optically thin, or moderately optically thick ($\tau \sim 0.6$ between 70–100 au in AS 209 and MWC 480). The column density for GM Aur is broadly constant at $\sim 10^{13}$ cm^2, while AS 209, HD 163296, and MWC 480 show broad peaks at values of ~ 5–8×10^{13} cm^{-2} and monotonic decreases with radius beyond ~100 au.

In summary, our radially resolved analysis shows much more variation across the sources than suggested by a simple disk-

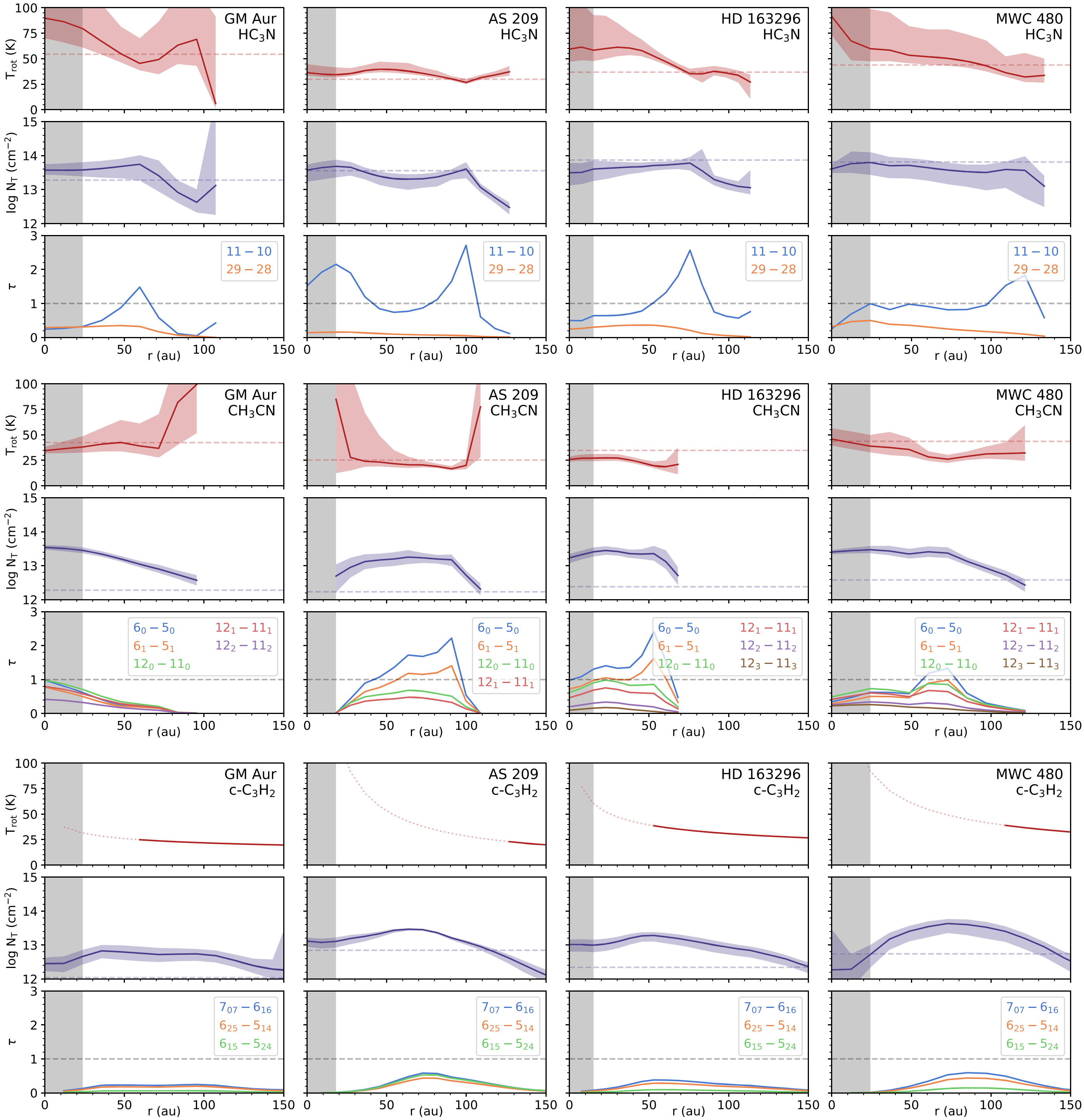

Figure 6. Radially resolved rotational diagrams for HC_3N (top), CH_3CN (middle), and c-C_3H_2 (bottom). Dashed lines indicate median values derived from the disk-integrated analysis (see Table 2) and $\tau = 1$. Gray shaded regions indicate a radial extent of 0.″15 (half of the beam size) within which quantities should be treated with caution. For c-C_3H_2, $T_{\rm rot}$ is fixed to the power-law fit of the ^{13}CO $J = 2$–1 temperature from Law et al. (2021b), with extrapolated values shown with a dotted line (see Section 3.4.2).

integrated analysis. Of particular note are the larger peak column densities extracted for CH_3CN and c-C_3H_2, and the high optical depth of the 11–10 and 6–5 transitions of HC_3N and CH_3CN, respectively, indicating that for these molecules the derived column densities in the inner disk may also be lower limits.

4. Discussion

The large range of information available from the multiple species and transitions targeted with MAPS enables us to probe further into the origin of the large organic molecules studied here.

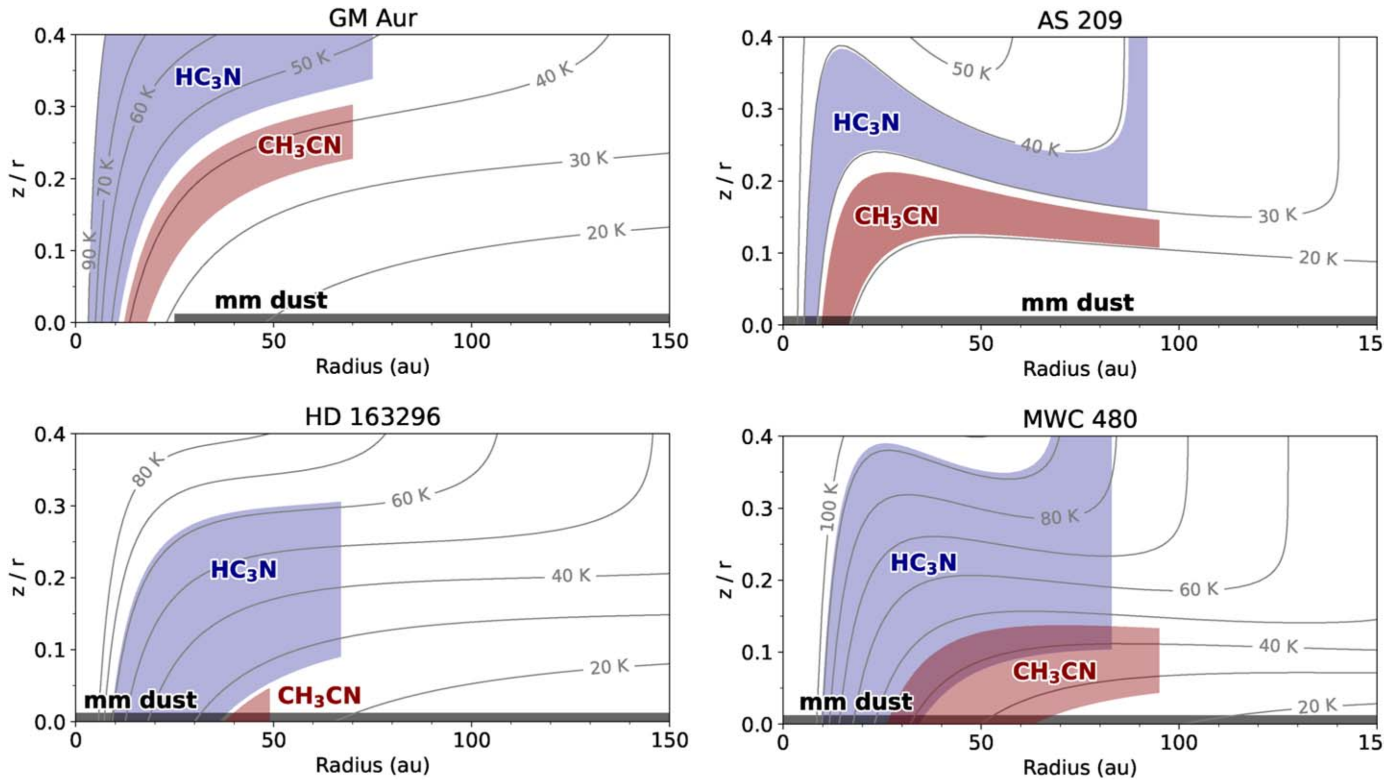

Figure 7. Two-dimensional disk temperature structures (contours) overlaid with the region of emission for HC_3N and CH_3CN along with the radial extent of the millimeter dust continuum emission at 220 GHz (see Section 4.1).

4.1. Distribution and Abundance of the Large Organics

We can use the results of our radially resolved rotation diagram analysis to further examine the origin of the emission from the large organic molecules. Law et al. (2021b) have determined two-dimensional temperature structures, $T(r, z)$, for each of our target disks based on fitting brightness temperatures from the mostly optically thick $J = 2–1$ transitions of ^{12}CO, ^{13}CO, and $C^{18}O$ isotopologues, based on the two-layer model of Dullemond et al. (2020). We can use this temperature structure to examine the spatial origin of the emission from these molecules in each of our disks. Under the assumption that the rotational temperature of each molecule is a measure of its true temperature (a sensible approximation given the high densities in protoplanetary disks), we can use the range of derived $T_{\rm rot}$ for each molecule from Figure 6 to map the range of heights in the disk from which the emission would originate. We can determine the radial range of emission following the approach of Law et al. (2021a) by calculating the radius encompassing 90% of flux in the radial profile from each molecule. Here, we measure this using the 0.″3 data for consistency with our previous analysis, but these only show minor differences with the results of Law et al. (2021a). Combining these radial (r) and height (z) bounds, we can determine the two-dimensional origin of the emission for each molecule, which is shown for each disk in Figure 7.

We note that the original $T(r, z)$ structure derived in Law et al. (2021b) is not a sensitive probe of the midplane temperature structure of the disks. This is because the CO emission from which these temperature structures are calculated originates from intermediate-to-high relative heights in the disks ($z/r \gtrsim 0.1$), and temperatures below 20 K were excluded from the fitting procedure. We have therefore renormalized the $T(r, z)$ structures such that the CO snowline (assumed to be 20 K) is reached at a midplane radius consistent with Zhang et al. (2021), whose thermochemical models reproduce both the SED and radial CO column density of each disk. We also note that we exclude the c-C_3H_2 emission from this comparison, since the rotational temperature we assume is not independent of the temperature structure derived from CO in each disk.

Our analysis of the origin of the line emission in $T(r, z)$ space reveals common trends across the four disks. In all cases, the HC_3N emission appears to originate from the highest temperature regime of the two molecules (∼30–80 K), and therefore at higher relative heights, generally in the range of $z/r = 0.1–0.4$. In contrast, the lower measured temperature of CH_3CN means it originates from lower relative heights, generally $z/r \lesssim 0.1–0.2$. The underlying differences in temperature structure between the warmer disks around Herbig stars (HD 163296 and MWC 480) and the cooler disks around T Tauri stars (GM Aur and AS 209) result in differences in the location of the emitting region of the molecules. In the cooler disks, the large organics primarily trace the warm molecular layer, and may only trace the disk midplane interior to 20 au. In the warmer disks, the large organics trace a wider radial range at the midplane interior to 60 au, and the warm molecular layer exterior to this. In particular, CH_3CN appears to originate almost exclusively from $z/r < 0.1$ in these warm disks. Nevertheless, the general morphology of the region of emission is similar for all disks—a region close to the midplane interior to the CO snowline, and an elevated warm molecular layer beyond it. Figure 4.1 also shows the extent of the 220 GHz dust continuum emission for each disk (see Sierra et al. 2021). This spans the full radial extent of the plots for each disk (with the exception of the inner ∼30 au for GM Aur), demonstrating that

Table 3
Large Organic Reservoir within 50 au for Each Disk

	Gas Mass			Gas+Ice Mass w.r.t. H_2O Ice [a]		
	HC_3N (10^{21} g)	CH_3CN (10^{21} g)	c-C_3H_2 (10^{21} g)	HC_3N (% H_2O)	CH_3CN (% H_2O)	c-C_3H_2 (% H_2O)
IM Lup	<0.01	<0.01	<0.01	<0.01	<0.01	<0.01
GM Aur	6.0	3.2	0.5	0.02	0.01	<0.01
AS 209	5.8	1.5	1.7	0.33	0.08	0.10
HD 163296	6.0	2.8	1.4	0.01	<0.01	<0.01
MWC 480	7.8	3.2	1.1	0.01	<0.01	<0.01

Note
[a] Assuming a 1000 to 1 ice-to-gas ratio and H_2O abundances from Zhang et al. (2021).

the edge of the millimeter dust in each disk is always exterior to edge of the large organic emission. This is in contrast to, e.g., H_2CO, which appears to be radially extended across all disks studied here (see Guzmán et al. 2021).

We can use the radial column density profiles to estimate the amount of each large organic molecule present in the inner 50 au of each disk (i.e., on scales comparable to the solar system) via conversion to a total surface density and integrating over the corresponding area. These values are listed in Table 3 (left). While there does not appear to an obvious trend for the gas mass of each large organic molecule between the disks (e.g., there appears to be no stellar mass dependence), it appears that HC_3N is significantly more abundant than either CH_3CN or c-C_3H_2 in each disk (by factors of 5–15). We can also estimate the total (gas and ice) mass of each of the large organics. Chemical models of these molecules in disks predict gas-to-ice ratios across a range of values, from 10^3 in Walsh et al. (2014) to 10^5 in Ruaud & Gorti (2019), so we conservatively adopt a 1000 to 1 ratio for our conversion. These values are also shown in Table 3 (right), expressed as a percentage of H_2O ice, estimated from predicted abundances in the thermochemical disk models of Zhang et al. (2021). This again demonstrates that HC_3N is most abundant in each disk. AS 209 emerges as a potential outlier, being particularly rich in large organics when compared to the other disks in our small sample by factors of ∼30 for HC_3N and ∼10 for both CH_3CN and c-C_3H_2. However, this may instead be due to a low modeled H_2O mass, and so observational constraints on this abundance would be required to confirm this.

4.2. Chemical Origin of the Large Organics

While determining the precise chemical origin of the large organic species will require dedicated models for each disk, we can use our empirically determined quantities to gain insight into general properties. Following Furuya & Aikawa (2014), we can estimate the typical temperature at which we would expect the large organic molecules to sublimate from icy grain surfaces into the gas phase. For gas densities in the range of 10^6–10^{12} cm^{-3}, we would expect this sublimation temperature to lie between 80–150 K.[26] It is therefore interesting that our derived rotational temperatures for HC_3N and CH_3CN (where we again note that the assumed rotational temperature of c-C_3H_2 is tied to the CO emission) are well below this value across the full radial extent of each disk. This suggests that, despite their close association with millimeter dust disk, these molecules cannot originate from direct thermal desorption (with the possible exception of the inner ∼20 au of GM Aur and MWC 480 for HC_3N, although uncertainties are large in these regions). Therefore, these species must be released from ices by nonthermal desorption processes (such as those triggered by cosmic rays and/or X-rays), or be formed in the gas phase directly.

We can also compare the column density ratios of simple and complex molecules in each disk to understand the efficiency of conversion from small to large organic species. Figure 8 shows the radially resolved ratio of column densities for HC_3N/HCN, CH_3CN/HCN, and c-C_3H_2/C_2H obtained from a comparison of our results with those of Guzmán et al. (2021). We indicate the regions across which our analysis of HC_3N or CH_3CN emission suggests $\tau > 1$, and thus where the column density ratio may be a lower limit. We also note that the derivation of HCN and C_2H column density is based on fitting the hyperfine transitions, and is not therefore influenced by the (large) optical depth of the main line component for these molecules. For the HC_3N/HCN ratio, all disks exhibit lower values in their inner ($\lesssim$50 au) regions of approximately 20% or less. Beyond radii at which the optical depth drops below 1 in GM Aur and HD 163296, the measured ratios increase sharply (even given the increase in associated uncertainties). The CH_3CN/HCN ratio broadly follows a similar pattern to that of the HC_3N/HCN, namely lower values ($\lesssim$5%) in the inner ($\lesssim$40–80 au) region. The CH_3CN/HCN ratio rises gradually in the outer regions of all disks, reaching values of 20–30% in the outer regions (>50 au) in all disks, where optical depths are below one. It is interesting to note that the general form of both the HC_3N/HCN and CH_3CN/HCN ratios as a function of radius (e.g., the sharp and shallow rise, respectively) are in agreement with the forward modeling retrieval performed by (Bergner et al. 2018, see their Figure 9).

In contrast to the nitriles, the c-C_3H_2/C_2H ratio is relatively flat across all radii in each of the disks at ∼5%. Increases of this ratio to levels of 15–20% are seen in the outer ($\gtrsim$100 au) regions of AS 209 and MWC 480. It is highly likely that c-C_3H_2 is a species that is formed purely in the gas phase in the atmospheres of protoplanetary disks similar to what is found in the interstellar medium (e.g., Loison et al. 2017). However, given the denser conditions within protoplanetary disks, a mechanism is required to maintain a source of carbon (chains) in the gas phase to seed such a chemistry, and this could potentially come from the nonthermal desorption of icy hydrocarbon precursors such as CH_4 and C_2H_6. Hence, this molecule is a counterexample to molecules such as CH_3CN for which it is known that both gas-phase and ice-phase chemistry are needed to explain its origin in protoplanetary disks (e.g., Loomis et al. 2018a). The flat profile of c-C_3H_2/C_2H within 100 au suggests that the gas-phase conversion of simple to complex hydrocarbons is relatively insensitive to radial location in these regions, and occurs at a similar rate in each disk in our sample.

Column density ratios of HC_3N/HCN and CH_3CN/HCN are have been calculated from remote observations of comets (while c-C_3H_2 has not been detected), allowing us to compare the relative chemical complexity of these disks with the organic material in the solar system. Biver & Bockelée-Morvan (2019) collate these values from numerous observations and find HC_3N/HCN ranges from ∼1–80%, and CH_3CN/HCN ranges from ∼3–45%, which we also show on Figure 8. The HC_3N/HCN ratio (or lower limit) is consistent with cometary

---

[26] Based on binding energies from KIDA: http://kida.obs.u-bordeaux1.fr.

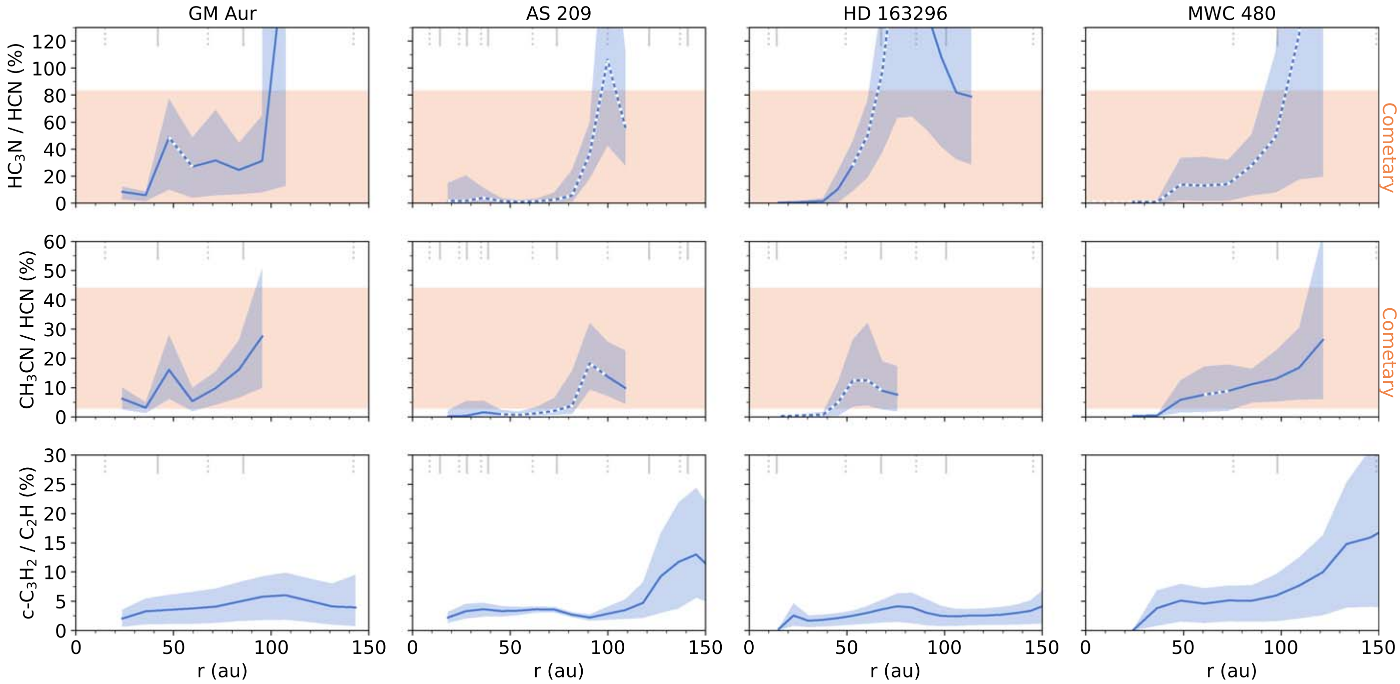

Figure 8. Ratio of column densities between the small (HCN, C_2H) and large organic molecules as derived from this work and Guzmán et al. (2021). Regions where our analysis suggests $\tau > 1$ are shown with a dashed line, and plots have been truncated in regions of low signal-to-noise. The range of observed values for solar system comets are shown by the vertical shaded regions (Biver & Bockelée-Morvan 2019, and references therein). Locations of continuum substructure (e.g., rings and gaps) are marked with gray vertical lines (solid and dotted, respectively).

measurements across all of the disks out to ∼100 au, and higher beyond this. The CH_3CN/HCN ratio is mostly consistent with cometary values, but the the inner regions of the AS 209, HD 163296, and MWC 480 disks are somewhat lower than the ratio measured in comets.

The expected formation zone of comets in the solar system is generally thought to be $\lesssim$40 au (see Mumma & Charnley 2011). The large-to-small organic ratios on these scales are difficult to probe in our target disks, due to the spatial resolution of our data (∼30–50 au). However, the general picture that emerges from this comparison is that the outer (50–100 au) regions of all disks are consistent with the composition of cometary material. In particular, the warmer HD 163296 and MWC 480 disks would likely have comet formation zones at correspondingly larger radii, and so this can be reconciled with a “scaled-up” picture of the solar system. If comets were to form in the outer regions of these disks ($\gtrsim$50–100 au), then they will attain a similar composition of nitriles to those observed in the solar system.

4.3. The (Lack of) Emission from IM Lup

An obvious outlier in our small sample is the IM Lup disk, which only exhibits tentative detections of CH_3CN and c-C_3H_2 and no detection of HC_3N. This is in contrast to firm detections of the smaller organic molecules discussed previously (Bergner et al. 2019; Guzmán et al. 2021), which demonstrate the precursors of the large organic molecules are at least present in this disk. IM Lup is the youngest star–disk system in our sample at 0.2–1.3 Myr old (Alcalá et al. 2017). If these large organic molecules are primarily formed *in situ* within the disk, then IM Lup may have not had sufficient time to build up a detectable gas-phase reservoir. This would be in broad agreement with dark cloud chemical models that demonstrate timescales of 10^5–10^6 yr are required to reach peak abundances for these species (see, e.g., Agúndez & Wakelam 2013). Alternatively, if the large organic molecules are primarily inherited from the protostellar phase (see, e.g., Drozdovskaya et al. 2016, 2019; Bianchi et al. 2019; Booth et al. 2021), then a short prestellar collapse phase would result in a lower abundance of these species in the disk.

The physical conditions of the IM Lup disk might also explain its lack of complex molecular emission. This disk has been found to be massive, with total disk mass estimates on the order of 0.17 $M_\odot$ (Cleeves et al. 2016). This density structure results in an optically thick region at Band 6 frequencies inside ∼50 au, which may be responsible for suppression of emission from CO isotopologues. A similar suppression of emission from other molecules should also occur, and if the emission originates from closer to the midplane (compared to CO), then this suppression may extend across a larger radial region. This scenario of flux deficit may explain the relative weakness of the large organic emission in IM Lup when compared to the other disks in our sample, and is in agreement with detailed studies of line emission from massive disks (Evans et al. 2019). Disentangling the relative importance of each of these processes on the resultant line emission from large molecules in IM Lup will require a detailed disk-specific model.

4.4. Comparison to Similar Observational Studies

Bergner et al. (2018) observed MWC 480 with ALMA and performed a rotational diagram analysis of large organic molecular emission. For HC_3N, they found a disk-integrated rotational temperature of 49 ± 6 K, similar to our derived value of $37.1^{+4.5}_{-2.9}$ K. However, their column density of $5.8 \pm 2.8 \times 10^{12}$ cm^{-2} is ∼13 times lower than the value we calculate here. This difference stems primarily from the differing spatial resolution of our data, with our 0.″3 observations able to place tighter constraints on the radial extent of the HC_3N emission for a disk-integrated analysis.

For CH_3CN, Bergner et al. (2018) find a disk-integrated column density of $1.8 \pm 0.4 \times 10^{12}$ cm^{-2}, which is similar to our value of $3.5^{+0.2}_{-0.2} \times 10^{12}$ cm^{-2}, but a rotational temperature of 73 ± 23 K, somewhat higher than our $48.6^{+5.7}_{-4.6}$ K. This could be reconciled if our observations are tracing different emitting layers; Bergner et al. (2018) observed transitions with $E_u \sim 150$–250 K, while our addition of the Band 3 data allows us access transitions down to $E_u = 20$ K.

Loomis et al. (2018a) observed several transitions of CH_3CN toward the T Tauri star TW Hya, performing a rotational diagram analysis across transitions spanning $E_u \sim 70$–150 K. They derive a disk-integrated column density of $1.45 \pm 0.2 \times 10^{12}$ cm^{-2} and rotational temperature of 32 ± 4 K. While the column density is comparable to our values across all disks, the rotational temperature is generally lower (with the exception of AS 209). This may be indicative of CH_3CN originating from a cooler region of the TW Hya disk compared to the objects studied here, or the result of a cooler disk more generally.

Qi et al. (2013) detected c-C_3H_2 toward HD 163296 using ALMA Science Verification data, finding a single-ring structure from ∼30–165 au. They derive a column density of $2.2 \pm 0.2 \times 10^{12}$ cm^{-2} at 100 au, which is very similar to our disk-integrated value. Cleeves et al. (2021) also recently reported a multi-line analysis of c-C_3H_2 toward TW Hya, and through a forward modeling approach found a best-fit column density of 1–3×10^{12} cm^{-2} with disk-integrated rotational temperatures for the ortho and para form of 55 ± 13 K and 43 ± 14 K, respectively. Such temperatures are comparable to our assumed values from ^{13}CO $J = 2$–1 between 50 and 100 au in three of our disks (with GM Aur being ∼10 K cooler), and the column density range is comparable to our disk-integrated values. However, our radially resolved column density values are a factor of ∼10–50 higher.

4.5. Comparison with Disk Chemical Models

Our observationally derived quantities can be compared to chemical models of protoplanetary disks. While disk-specific models encompassing the full chemistry required to explain the abundances of these molecules are not yet available, more general disk chemical models are still informative. Walsh et al. (2014) studied the composition of a representative disk around a T Tauri star with a large gas-grain complex chemical network that included both HC_3N and CH_3CN. Their spatial distribution of gaseous HC_3N and CH_3CN is characterized by an inner, warm component reaching down to the midplane along with a population of molecules found at higher relative heights ($z/r \gtrsim 0.2$) for larger radii. While the scales differ, such a morphology is in broad agreement with our derived origin of the line emission in Figure 7, though dedicated radiative transfer modeling would be needed to determine those regions of the disk that contribute the most to the emergent flux for the transitions studied here.

We can also compare our derived molecular abundances to their model via our radially resolved N_T profiles. Across our disk sample, peak N_T(HC_3N) are between 10^{13}–10^{14} cm^{-2} within ∼100 au, but are likely lower limits due to the high optical depth discussed above. Such values are up to 500 times higher than the HC_3N column densities seen in the Walsh et al. (2014) model at similar radii, and even ∼100 times higher than those at 10 au (see their Figure 8 and Table 2). A less extreme picture emerges when comparing the N_T(CH_3CN), where our derived values are ∼5–10 times higher than those in the model between 10 and 100 au. Exploring the chemical structure as a function of height at a radius of 300 au, Walsh et al. (2014) also found that models including only gas-phase chemistry result in the largest fractional abundance of HC_3N achieved in the disk atmosphere, whereas models in which grain-surface (ice) chemistry was included achieved the largest fractional abundance of gas-phase CH_3CN. This demonstrates the importance of a complete treatment of both gas- and ice-phase reactions in such models.

More recently, Le Gal et al. (2019) investigated the effect of changes in C/O ratio in a protoplanetary disk on the resulting abundances of nitrile species including HC_3N and CH_3CN. Their peak column densities for both species (that require C/O = 1.0 and the inclusion of grain-surface formation routes) are approximately 10^{12} cm^{-2}, still a factor of 10–100 smaller than the column densities we derive across our disk sample. Wakelam et al. (2019) recently explored the impact on vertically integrated column densities of molecules in protoplanetary disks excluding and including the effects of dust growth and settling on the disk structure and chemistry and also including ice chemistry. Of particular interest for our work is the sensitivity of the column density values and distribution of HC_3N. In their fiducial models (no grain growth nor settling), they achieve column densities $\gtrsim 10^{12}$ cm^{-2} only within the inner 20 au, with a typical column density of $\sim 10^{11}$–10^{12} cm^{-2} obtained in the outer disk, and increasing with radius. This is similar to the results of Walsh et al. (2014). However, in models where grain growth and settling are included, they obtain an increase on the order of 1 to 2 orders of magnitude in the column density of HC_3N in the outer disk. The model that obtains the highest peak column density is also a model that begins the chemistry with atomic initial abundances, rather than molecular, indicating also the importance of having free carbon available in the gas phase for the formation of carbon-rich molecules with gas-phase formation pathways such as HC_3N, despite the bulk gas possessing elemental ratio of C/O < 1. It is not specifically explained why dust growth and settling boosts the formation of HC_3N; however, it may to be related to the decrease in altitude of the dust photosphere allowing greater penetration of bond-breaking radiation that then drives a rich gas-phase chemistry.

The broad picture that emerges from the above comparisons is that current static chemical models generally underpredict the abundance of HC_3N and CH_3CN by a significant margin. Only in the case of a gas-grain chemical model that also includes dust growth and settling does the column density, specifically of HC_3N, approach the values derived here (Wakelam et al. 2019). It is also noteworthy that the static models presented in Loomis et al. (2018a) are able to reproduce the radial column density of CH_3CN in TW Hya well, but only when both gas-phase and ice-phase chemistry are included, along with a high photodesorption rate.

Beyond an incomplete picture of chemical formation pathways, it is possible that the above disk chemical models are not complete in their description of physical processes that could cause a higher abundance of organic molecules. For example, the radial drift of large ($\gtrsim$ millimeter-sized) grains from the outer regions of the disk can alter the chemical composition of the inner regions, which may manifest in one of two different ways. If a molecule is formed primarily via grain-surface reactions, then the radial drift of grains will lead to an enhancement of gas-phase abundance within the relevant ice line (see, e.g., Booth et al. 2017). However, if the organic molecule is produced more readily in the gas phase, then radial drift may still play a role. The redistribution of bulk carriers of major elements via radial drift will alter elemental ratios in the inner disk (for example, C/O; see, e.g., Piso et al. 2015) that can alter the formation efficiency of molecules such as HC_3N and CH_3CN (as demonstrated by Le Gal et al. 2019). Quantifying the detailed effects of these dust transport processes on the distribution of large molecules would require coupled models that include radial drift of dust and gas-grain chemical kinetics. While such models employing small chemical networks are beginning to emerge (see, e.g., Booth & Ilee 2019), they have not yet been expanded to include the reactions required to track the chemical evolution of larger molecules.

In addition to the radial motions of solids, vertical motions of gas and dust could also act to alter the abundances of molecules in a disk. Semenov & Wiebe (2011) modeled the chemical evolution of a disk including turbulent transport of gas and dust in the form of turbulent diffusion. They find that the column densities of species we study here—HC_3N, CH_3CN, and c-C_3H_2—can be enhanced by up to factors of 10–20 in the case of a fast mixing scenario compared with a static disk. This enhancement occurs when grains with icy mantles are transported from the disk midplane to warmer vertical layers, causing heavy radical species in the ices to become more mobile. This leads to the production of more complex molecules on the grain surfaces, which are then released into the gas. Models presented in Öberg et al. (2015) to aid the interpretation of the first detections of HC_3N and CH_3CN in MWC 480 also explored the impact of vertical mixing driven by turbulence on the column densities of both species. While high levels of turbulence are in tension with current measurements in the line-emitting regions of protoplanetary disks ($\alpha \lesssim 10^{-3}$; e.g., Flaherty et al. 2020) and observations of well-settled millimeter dust (Villenave et al. 2020), it was shown that even models with low levels of turbulent mixing better-reproduced the column densities derived from observations. It is also possible that mixing is driven via local mechanisms such as meridional flows generated by the accretion of embedded planets (Teague et al. 2019); however, the impact of this is yet to be investigated in chemical models of protoplanetary disks.

4.6. Future Outlook

Despite the impressive diagnostic power of the MAPS observations we present here, it is clear that we are operating at the limits of the data. For the weakest transitions (e.g., CH_3CN 6–5) we are primarily limited by sensitivity, and so future observational campaigns aiming to characterize larger molecules in disks should be designed with this in mind. We have shown that the combination of observations for transitions spanning a large range of upper state energy are particularly powerful, and so this should also be maximized. Further characterization of the gas substructure for the brighter transitions (e.g., c-C_3H_2 7_{07}–6_{16}) would benefit from deeper, higher angular resolution studies, which may elucidate any (anti)correlations with the millimeter dust substructures that are so well characterized in these disks. Our findings also demonstrate that the current state of the art for protoplanetary disk chemical models may require extension if they are to explain the latest observations. Whether this extension requires the addition of further physical or chemical processes remains to be seen. Nevertheless, it is clear that high angular resolution and sensitivity observations are essential in order to further our understanding of the complex chemistry in disks.

5. Summary

In this work, we have analyzed observations of the large organic molecules HC_3N, CH_3CN, and c-C_3H_2 toward five protoplanetary disks as part of the ALMA MAPS Large Program. We summarize our findings below:

1. We robustly detect multiple transitions of HC_3N, CH_3CN, and c-C_3H_2 in AS 209, GM Aur, HD 163296, and MWC 480. For IM Lup, we only tentatively detect single transitions of c-C_3H_2 and CH_3CN.
2. There appears to be a weak relationship between millimeter dust morphology and the morphology of line emission from these molecules. There are no disk-wide trends between, for example, the depletion of millimeter dust and the depletion of any molecule in the gas (with the possible exception of c-C_3H_2 in AS 209, HD 163296, and MWC 480).
3. Disk-integrated column densities and temperatures are broadly consistent with previous observational studies, where available. However, the high angular resolution of our observations allows us to investigate radially resolved properties, revealing a significant increase in molecular column density for HC_3N and CH_3CN at small radii. Emission from these molecules appears to be optically thick within 50–100 au in all disks, suggesting that these higher column densities are likely lower limits.
4. The emission in all disks is compact ($\lesssim$100 au) and close to the extent of the millimeter dust disk, suggesting that the ice reservoirs hosted on grains may play a role in the formation of these species. However, the derived rotational temperatures are below the expected sublimation temperatures for each of the molecules, ruling out thermal desorption as an origin.
5. Comparison with existing disk chemical models shows that static models cannot generally reproduce the high column densities we observe. In contrast, chemical models that include dynamic processes such as radial drift and vertical mixing could explain larger column densities that we observe in these disks.
6. We approximate the two-dimensional (r, z) locations where we expect the molecules to emit, finding that CH_3CN originates from close to the midplane in all disks ($z/r \lesssim 0.1$), while HC_3N originates in higher layers ($z/r \sim 0.1$–0.4). This is consistent with distributions predicted by disk chemical models. In addition, we find that emission occurs at higher z/r in the disks around T Tauri stars when compared with those around the Herbig stars.
7. We find good agreement between relative abundances of simple and complex nitrile species in the outer regions of each disk, and with remote observations of solar system comets. The conversion efficiency of small to large hydrocarbons appears to be low (5–10%) and generally insensitive to radial location within the disks.

We have demonstrated that four of the protoplanetary disks studied here—GM Aur, AS 209, HD 163296, and MWC 480—all contain significant reservoirs of the large organic molecules

HC_3N, CH_3CN, and c-C_3H_2 on scales comparable with the extent of their millimeter dust disks. These dust disks all host rings and gaps, and HD 163296 and MWC 480 exhibit deviations from Keplerian velocities in their CO gas emission (Teague et al. 2021). In many cases, these phenomena can be readily explained by the presence of forming planets. Our analysis also shows that these molecules can emit from close to the disk midplane (particularly for the disks around the Herbig stars), where the majority of planet formation processes operate. Our results are therefore consistent with a picture in which the precursors to biologically relevant molecules are abundant in the raw material available for planet formation in protoplanetary disks, and that this material can have a composition similar to that within our own solar system.

We are grateful to the anonymous referee for a constructive report that improved the clarity of the manuscript. This paper makes use of the following ALMA data: ADS/JAO. ALMA#2018.1.01055.L. ALMA is a partnership of ESO (representing its member states), NSF (USA) and NINS (Japan), together with NRC (Canada), MOST and ASIAA (Taiwan), and KASI (Republic of Korea), in cooperation with the Republic of Chile. The Joint ALMA Observatory is operated by ESO, AUI/NRAO and NAOJ. The National Radio Astronomy Observatory is a facility of the National Science Foundation operated under cooperative agreement by Associated Universities, Inc.

J.D.I. acknowledges support from the Science and Technology Facilities Council of the United Kingdom (STFC) under ST/T000287/1. C.W. acknowledges financial support from the University of Leeds, STFC and UKRI (grant Nos. ST/R000549/1, ST/T000287/1, MR/T040726/1). A.S.B acknowledges the studentship funded by the Science and Technology Facilities Council of the United Kingdom (STFC). Y.A. acknowledges support by NAOJ ALMA Scientific Research grant code 2019-13B, and grant-in-Aid for Scientific Research 18H05222 and 20H05847. S.M.A. and J.H. acknowledge funding support from the National Aeronautics and Space Administration under grant No. 17-XRP17 2-0012 issued through the Exoplanets Research Program. J.B. acknowledges support by NASA through the NASA Hubble Fellowship grant No. HST-HF2-51427.001-A awarded by the Space Telescope Science Institute, which is operated by the Association of Universities for Research in Astronomy, Incorporated, under NASA contract NAS5-26555. E.A.B. and A.D.B. acknowledge support from NSF AAG grant No. 1907653. J.B.B. acknowledges support from NASA through the NASA Hubble Fellowship grant No. HST-HF2-51429.001-A, awarded by the Space Telescope Science Institute, which is operated by the Association of Universities for Research in Astronomy, Inc., for NASA, under contract NAS5-26555. G.C. is supported by NAOJ ALMA Scientific Research grant code 2019-13B. L.I.C. gratefully acknowledges support from the David and Lucille Packard Foundation and Johnson & Johnson's WiSTEM2D Program. I.C. was supported by NASA through the NASA Hubble Fellowship grant HST-HF2-51405.001-A awarded by the Space Telescope Science Institute, which is operated by the Association of Universities for Research in Astronomy, Inc., for NASA, under contract NAS5-26555. V.V. G. acknowledges support from FONDECYT Iniciación 11180904 and ANID project Basal AFB-170002. J.H. acknowledges support for this work provided by NASA through the NASA Hubble Fellowship grant No. HST-HF2-51460.001-A awarded by the Space Telescope Science Institute, which is operated by the Association of Universities for Research in Astronomy, Inc., for NASA, under contract NAS5-26555. C.J.L. acknowledges funding from the National Science Foundation Graduate Research Fellowship under grant DGE1745303. R.L.G. acknowledges support from a CNES fellowship grant. F.M. acknowledges support from ANR of France under contract ANR-16-CE31-0013 (Planet-Forming-Disks) and ANR-15-IDEX-02 (through CDP "Origins of Life"). H.N. acknowledges support by NAOJ ALMA Scientific Research grant code 2018-10B and Grant-in-Aid for Scientific Research 18H05441. K.I.Ö. acknowledges support from the Simons Foundation (SCOL No. 321183) and an NSF AAG grant (No. 1907653). K.R.S. acknowledges the support of NASA through Hubble Fellowship Program grant HST-HF2-51419.001, awarded by the Space Telescope Science Institute,which is operated by the Association of Universities for Research in Astronomy, Inc., for NASA, under contract NAS5-26555. R.T. acknowledges support from the Smithsonian Institution as a Submillimeter Array (SMA) Fellow. T.T. is supported by JSPS KAKENHI grant Numbers JP17K14244 and JP20K04017. Y.Y. is supported by IGPEES, WINGS Program, the University of Tokyo. K.Z. acknowledges the support of the Office of the Vice Chancellor for Research and Graduate Education at the University of Wisconsin–Madison with funding from the Wisconsin Alumni Research Foundation, and the support of NASA through Hubble Fellowship grant HST-HF2-51401.001. awarded by the Space Telescope Science Institute, which is operated by the Association of Universities for Research in Astronomy, Inc., for NASA, under contract NAS5-26555.

Facility: ALMA.

Software: CASA (McMullin et al. 2007), Astropy (Astropy Collaboration et al. 2013), Matplotlib (Hunter 2007), NumPy (Harris et al. 2020), emcee (Foreman-Mackey et al. 2013), bettermoments (Teague & Foreman-Mackey 2018), GoFish (Teague 2019), VISIBLE (Loomis et al. 2018b).

Appendix A
Gallery of Integrated Intensity (Zeroth Moment) Maps

Figures 9, 10, and 11 show the integrated intensity maps for all disks and transitions studied in this work.

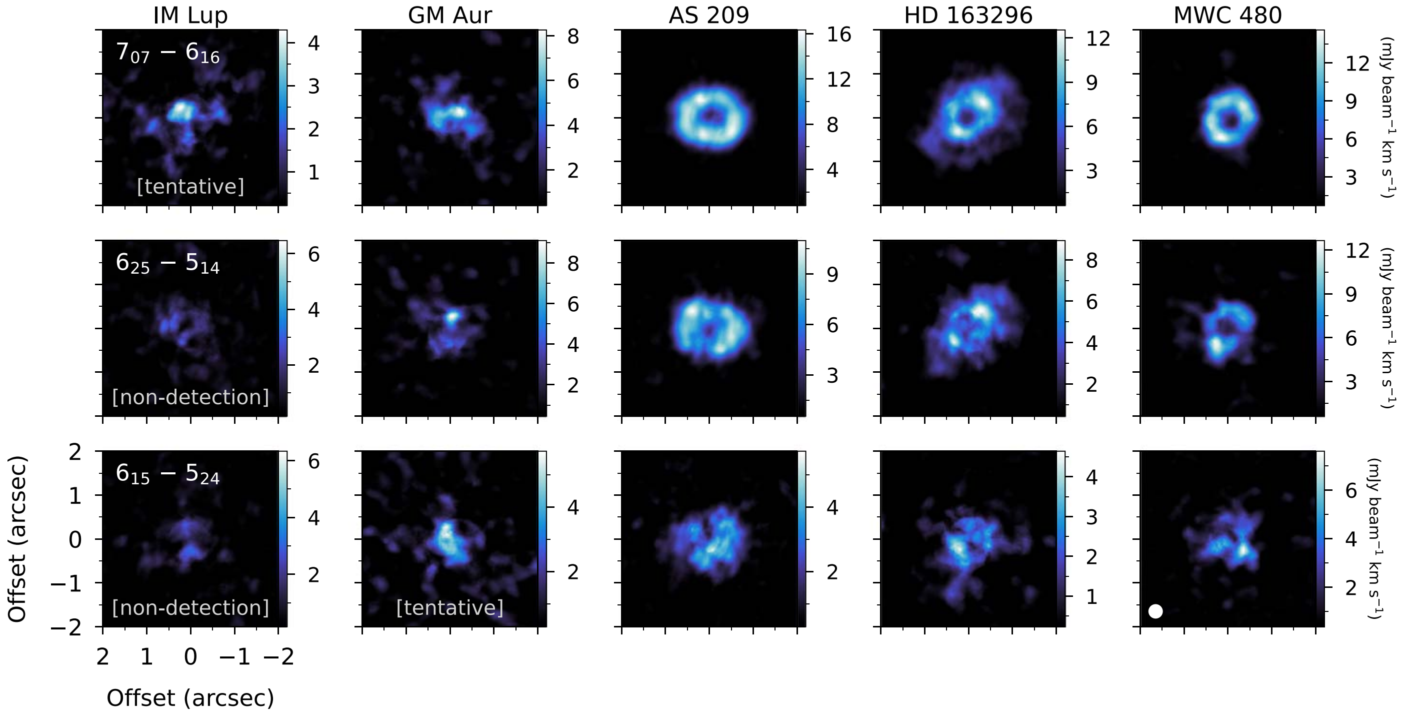

Figure 9. Integrated intensity (zeroth moment) maps for transitions of c-C_3H_2.

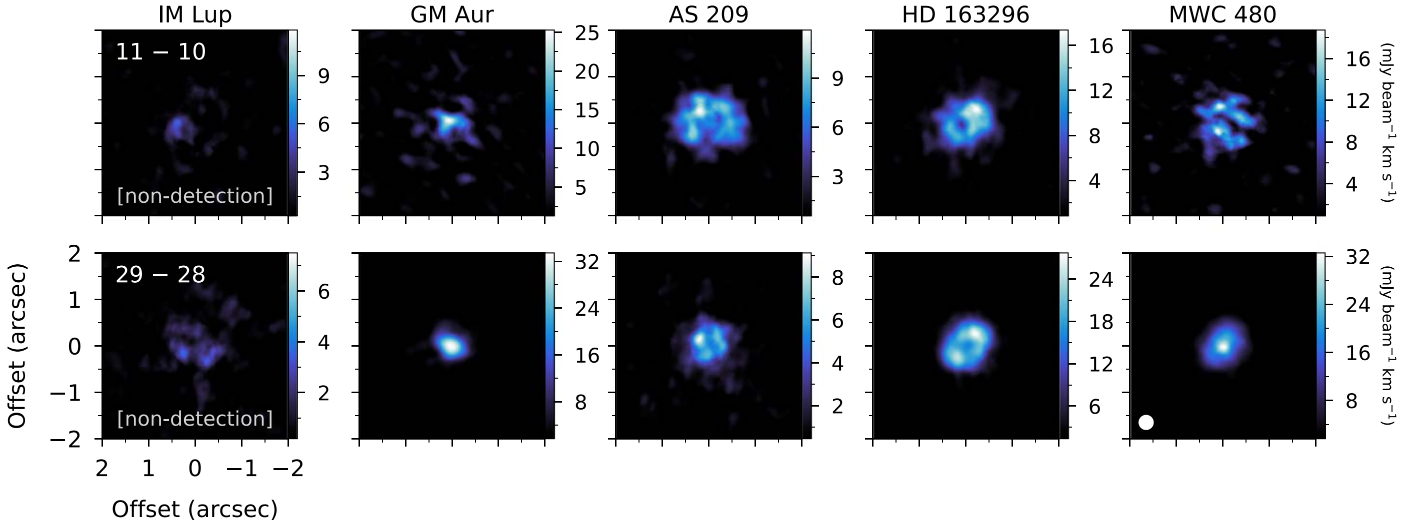

Figure 10. Integrated intensity (zeroth moment) maps for transitions of HC_3N.

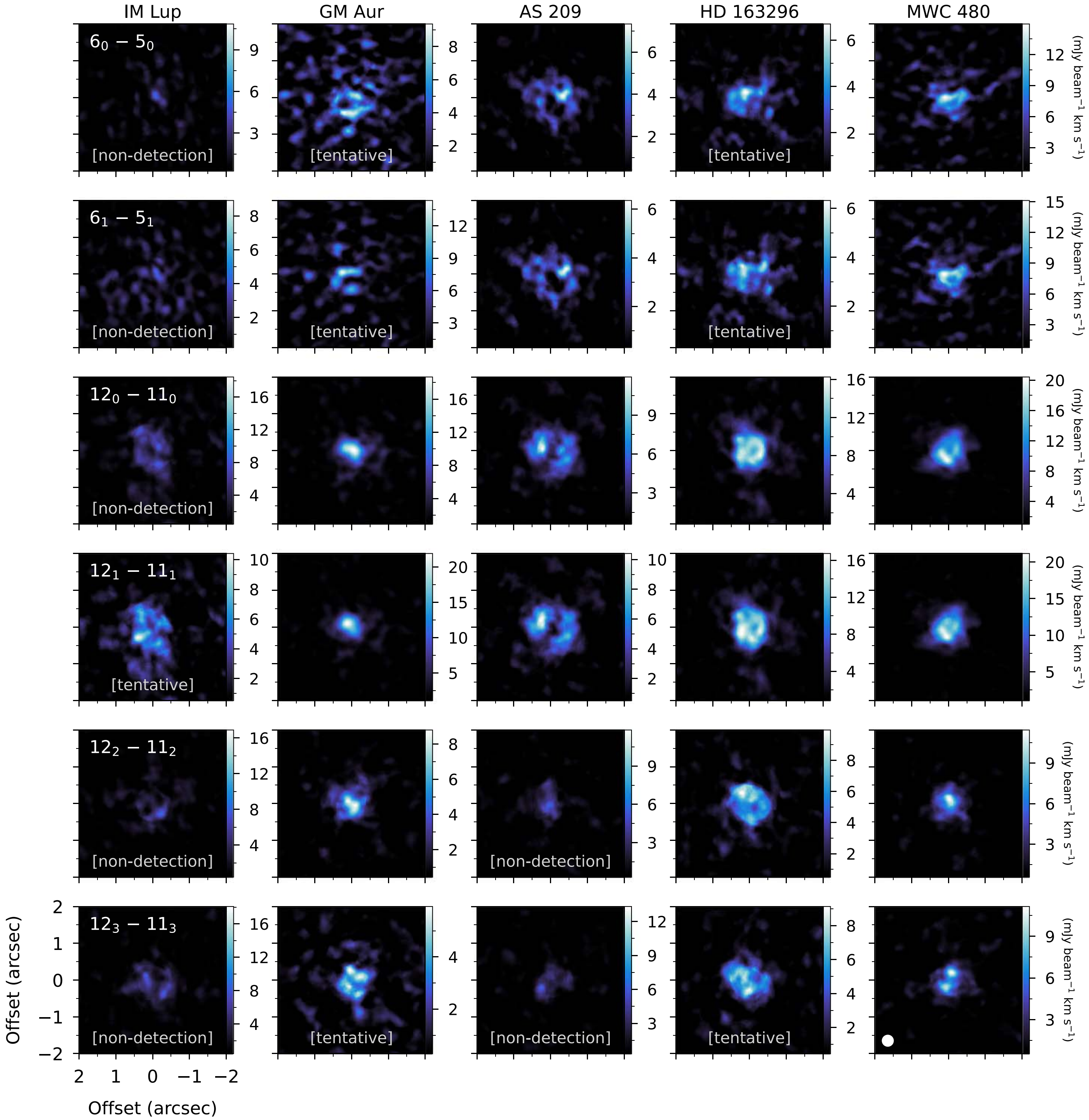

Figure 11. Integrated intensity (zeroth moment) maps for transitions of CH_3CN.

Appendix B
Molecular Data

Table 4 details the molecular spectroscopic data and constants that have been used throughout this work.

Table 4
List of Transitions and Associated Molecular Spectroscopic Data, Taken from the CDMS[a]

Transition	Quantum Numbers	Frequency (GHz)	E_u (K)	$\log_{10}(A_{ij}/s^{-1})$	g_u
HC_3N					
11–10	$J = 11–10$	100.0763920	28.8	−4.1096	23
29–28	$J = 29–28$	263.7923080	189.9	−2.8349	59
CH_3CN					
$6_5–5_5$	$J = 6–5, K = 5$	110.3303454	197.1	−4.4697	26
$6_4–5_4$	$J = 6–5, K = 4$	110.3494707	132.8	−4.2098	26
$6_3–5_3$	$J = 6–5, K = 3$	110.3643540	82.8	−4.0792	52
$6_2–5_2$	$J = 6–5, K = 2$	110.3749894	47.1	−4.0054	26
$6_1–5_1$	$J = 6–5, K = 1$	110.3813723	25.7	−3.9664	26
$6_0–5_0$	$J = 6–5, K = 0$	110.3835002	18.5	−3.9542	26
$12_4–11_4$	$J = 12–11, K = 4$	220.6792874	183.1	−3.0857	50
$12_3–11_3$	$J = 12–11, K = 3$	220.7090174	133.2	−3.0624	100
$12_2–11_2$	$J = 12–11, K = 2$	220.7302611	97.4	−3.0465	50
$12_1–11_1$	$J = 12–11, K = 1$	220.7430111	76.0	−3.0372	50
$12_0–11_0$	$J = 12–11, K = 0$	220.7472617	68.9	−3.0342	50
c-C_3H_2					
$7_{07}–6_{16}$[b]	$J = 7–6, K_a = 0–1, K_c = 7–6$	251.3143670	50.7	−3.0704	45
$6_{15}–5_{24}$	$J = 6–5, K_a = 1–2, K_c = 5–4$	251.5087085	47.5	−3.1706	13
$6_{25}–5_{14}$	$J = 6–5, K_a = 2–1, K_c = 5–4$	251.5273110	47.5	−3.1708	39

Notes

[a] https://cdms.astro.uni-koeln.de/cdms/portal/

[b] Includes blended para transition ($7_{17}–6_{06}$) at the same frequency; see Section 3.4.

Appendix C
Disk Temperature Structures

Table 5 details the disk temperature structures that have been adopted during the rotational analysis of the c-C_3H_2 emission. For further details, see Law et al. (2021b).

Table 5
Summary of Parameters Used for the Temperature Structures of the Disks (see Law et al. 2021b)

	IM Lup	GM Aur	AS 209	HD 163296	MWC 480
$T(r)$ parameters (^{13}CO $J = 2–1$):					
$r_{\text{fit, in}}$ (au)	145	50	125	50	100
$r_{\text{fit, out}}$ (au)	339	314	163	356	388
T_{100} (K)	30 ± 0.6	22 ± 0.2	28 ± 1.3	31 ± 0.2	42 ± 0.9
q	0.323 ± 0.03	0.260 ± 0.01	0.804 ± 0.13	0.367 ± 0.01	0.598 ± 0.03
$T(r, z)$ parameters:					
$T_{\text{atm},0}$ (K)	$36^{+0.1}_{-0.1}$	$48^{+0.3}_{-0.3}$	$37^{+0.2}_{-0.2}$	$63^{+0.2}_{-0.2}$	$69^{+0.2}_{-0.2}$
$T_{\text{mid},0}$ (K)	$25^{+0.1}_{-0.1}$	$20^{+0.2}_{-0.2}$	$25^{+0.2}_{-0.2}$	$24^{+0.1}_{-0.1}$	$27^{+0.2}_{-0.2}$

ORCID iDs

John D. Ilee https://orcid.org/0000-0003-1008-1142
Catherine Walsh https://orcid.org/0000-0001-6078-786X
Alice S. Booth https://orcid.org/0000-0003-2014-2121
Yuri Aikawa https://orcid.org/0000-0003-3283-6884
Sean M. Andrews https://orcid.org/0000-0003-2253-2270
Jaehan Bae https://orcid.org/0000-0001-7258-770X
Edwin A. Bergin https://orcid.org/0000-0003-4179-6394
Jennifer B. Bergner https://orcid.org/0000-0002-8716-0482
Arthur D. Bosman https://orcid.org/0000-0003-4001-3589
Gianni Cataldi https://orcid.org/0000-0002-2700-9676
L. Ilsedore Cleeves https://orcid.org/0000-0003-2076-8001
Ian Czekala https://orcid.org/0000-0002-1483-8811
Viviana V. Guzmán https://orcid.org/0000-0003-4784-3040
Jane Huang https://orcid.org/0000-0001-6947-6072
Charles J. Law https://orcid.org/0000-0003-1413-1776
Romane Le Gal https://orcid.org/0000-0003-1837-3772
Ryan A. Loomis https://orcid.org/0000-0002-8932-1219
François Ménard https://orcid.org/0000-0002-1637-7393
Hideko Nomura https://orcid.org/0000-0002-7058-7682
Karin I. Öberg https://orcid.org/0000-0001-8798-1347
Chunhua Qi https://orcid.org/0000-0001-8642-1786
Kamber R. Schwarz https://orcid.org/0000-0002-6429-9457
Richard Teague https://orcid.org/0000-0003-1534-5186
Takashi Tsukagoshi https://orcid.org/0000-0002-6034-2892
David J. Wilner https://orcid.org/0000-0003-1526-7587
Yoshihide Yamato https://orcid.org/0000-0003-4099-6941
Ke Zhang https://orcid.org/0000-0002-0661-7517

References

Agúndez, M., & Wakelam, V. 2013, ChRv, 113, 8710
Aikawa, Y., Momose, M., Thi, W.-F., et al. 2003, PASJ, 55, 11
Aikawa, Y., van Zadelhoff, G. J., van Dishoeck, E. F., & Herbst, E. 2002, A&A, 386, 622
Alarcón, F., Teague, R., Zhang, K., Bergin, E. A., & Barraza-Alfaro, M. 2020, ApJ, 905, 68
Alcalá, J. M., Manara, C. F., Natta, A., et al. 2017, A&A, 600, A20
Altwegg, K., Balsiger, H., & Fuselier, S. A. 2019, ARA&A, 57, 113
Astropy Collaboration, Robitaille, T. P., Tollerud, E. J., et al. 2013, A&A, 558, A33
Bergin, E. A., Du, F., Cleeves, L. I., et al. 2016, ApJ, 831, 101
Bergner, J. B., Guzmán, V. G., Öberg, K. I., Loomis, R. A., & Pegues, J. 2018, ApJ, 857, 69
Bergner, J. B., Öberg, K. I., Bergin, E. A., et al. 2019, ApJ, 876, 25
Bianchi, E., Codella, C., Ceccarelli, C., et al. 2019, MNRAS, 483, 1850
Biver, N., & Bockelée-Morvan, D. 2019, ESC, 3, 1550
Booth, A. S., Walsh, C., Terwisscha van Scheltinga, J., et al. 2021, NatAs, 5, 684
Booth, R. A., Clarke, C. J., Madhusudhan, N., & Ilee, J. D. 2017, MNRAS, 469, 3994
Booth, R. A., & Ilee, J. D. 2019, MNRAS, 487, 3998
Carney, M. T., Hogerheijde, M. R., Guzmán, V. V., et al. 2019, A&A, 623, A124
Caselli, P., & Ceccarelli, C. 2012, A&ARv, 20, 56
Chapillon, E., Dutrey, A., Guilloteau, S., et al. 2012, ApJ, 756, 58
Cleeves, L. I., Loomis, R. A., Teague, R., et al. 2021, ApJ, 911, 29
Cleeves, L. I., Öberg, K. I., Wilner, D. J., et al. 2016, ApJ, 832, 110
Czekala, I., Loomis, R. A., Teague, R., et al. 2021, ApJS, 257, 2
Drozdovskaya, M. N., van Dishoeck, E. F., Rubin, M., Jørgensen, J. K., & Altwegg, K. 2019, MNRAS, 490, 50
Drozdovskaya, M. N., Walsh, C., van Dishoeck, E. F., et al. 2016, MNRAS, 462, 977
Du, F., Bergin, E. A., Hogerheijde, M., et al. 2017, ApJ, 842, 98
Dullemond, C. P., Isella, A., Andrews, S. M., Skobleva, I., & Dzyurkevich, N. 2020, A&A, 633, A137
Dutrey, A., Guilloteau, S., & Guelin, M. 1997, A&A, 317, L55
Evans, M. G., Hartquist, T. W., Caselli, P., et al. 2019, MNRAS, 483, 1266
Facchini, S., Pinilla, P., van Dishoeck, E. F., & de Juan Ovelar, M. 2018, A&A, 612, A104
Facchini, S., Teague, R., Bae, J., et al. 2021, AJ, 162, 99
Favre, C., Fedele, D., Semenov, D., et al. 2018, ApJL, 862, L2
Flaherty, K., Hughes, A. M., Simon, J. B., et al. 2020, ApJ, 895, 109
Flaherty, K. M., Hughes, A. M., Rosenfeld, K. A., et al. 2015, ApJ, 813, 99
Foreman-Mackey, D., Hogg, D. W., Lang, D., & Goodman, J. 2013, PASP, 125, 306
Furuya, K., & Aikawa, Y. 2014, ApJ, 790, 97
Garufi, A., Podio, L., Codella, C., et al. 2021, A&A, 645, A145
Goldsmith, P. F., & Langer, W. D. 1999, ApJ, 517, 209
Guzmán, V. V., Bergner, J. B., Law, C. J., et al. 2021, ApJS, 257, 6
Guzmán, V. V., Huang, J., Andrews, S. M., et al. 2018b, ApJL, 869, L48
Guzmán, V. V., Öberg, K. I., Carpenter, J., et al. 2018a, ApJ, 864, 170
Harris, C. R., Millman, K. J., van der Walt, S. J., et al. 2020, Natur, 585, 357
Herbst, E., & van Dishoeck, E. F. 2009, ARA&A, 47, 427
Hunter, J. D. 2007, CSE, 9, 90
Isella, A., Huang, J., Andrews, S. M., et al. 2018, ApJL, 869, L49
Jorgensen, J. K., Belloche, A., & Garrod, R. T. 2020, ARA&A, 58, 727
Jorsater, S., & van Moorsel, G. A. 1995, AJ, 110, 2037
Kama, M., Bruderer, S., van Dishoeck, E. F., et al. 2016, A&A, 592, A83
Kastner, J. H., Qi, C., Dickson-Vandervelde, D. A., et al. 2018, ApJ, 863, 106
Kastner, J. H., Zuckerman, B., Weintraub, D. A., & Forveille, T. 1997, Sci, 277, 67
Law, C., Loomis, R. A., Teague, R., et al. 2021a, ApJS, 257, 3
Law, C., Teague, R., Loomis, R. A., et al. 2021b, ApJS, 257, 4
Le Gal, R., Brady, M. T., Öberg, K. I., Roueff, E., & Le Petit, F. 2019, ApJ, 886, 86
Lee, J.-E., Lee, S., Baek, G., et al. 2019, NatAs, 3, 314
Loison, J.-C., Agúndez, M., Wakelam, V., et al. 2017, MNRAS, 470, 4075
Loomis, R. A., Cleeves, L. I., Öberg, K. I., et al. 2018a, ApJ, 859, 131
Loomis, R. A., Öberg, K. I., Andrews, S. M., et al. 2018b, AJ, 155, 182
Loomis, R. A., Öberg, K. I., Andrews, S. M., et al. 2020, ApJ, 893, 101
McMullin, J. P., Waters, B., Schiebel, D., Young, W., & Golap, K. 2007, in ASP Conf. Ser. 376, Astronomical Data Analysis Software and Systems XVI, ed. R. A. Shaw, F. Hill, & D. J. Bell (San Francisco, CA: ASP), 127
Müller, H. S. P., Schlöder, F., Stutzki, J., & Winnewisser, G. 2005, JMoSt, 742, 215
Mumma, M. J., & Charnley, S. B. 2011, ARA&A, 49, 471
Öberg, K. I., Guzmán, V. V., Furuya, K., et al. 2015, Natur, 520, 198
Öberg, K. I., Guzmán, V. V., Walsh, C., et al. 2021, ApJS, 257, 1
Öberg, K. I., Qi, C., Fogel, J. K. J., et al. 2010, ApJ, 720, 480
Pegues, J., Öberg, K. I., Bergner, J. B., et al. 2020, ApJ, 890, 142
Piso, A.-M. A., Öberg, K. I., Birnstiel, T., & Murray-Clay, R. A. 2015, ApJ, 815, 109
Podio, L., Garufi, A., Codella, C., et al. 2020, A&A, 642, L7
Qi, C., Öberg, K. I., Wilner, D. J., & Rosenfeld, K. A. 2013, ApJL, 765, L14
Ruaud, M., & Gorti, U. 2019, ApJ, 885, 146
Semenov, D., & Wiebe, D. 2011, ApJS, 196, 25
Sierra, A., Pérez, L. M., Zhang, K., et al. 2021, ApJS, 257, 14
Spezzano, S., Tamassia, F., Thorwirth, S., et al. 2012, ApJS, 200, 1
Teague, R. 2019, JOSS, 4, 1632
Teague, R., Bae, J., Aikawa, Y., et al. 2021, ApJS, 257, 18
Teague, R., Bae, J., & Bergin, E. A. 2019, Natur, 574, 378
Teague, R., & Foreman-Mackey, D. 2018, RNAAS, 2, 173
Terwisscha van Scheltinga, J., Hogerheijde, M. R., Cleeves, L. I., et al. 2021, ApJ, 906, 111
Thi, W. F., van Zadelhoff, G. J., & van Dishoeck, E. F. 2004, A&A, 425, 955
van der Marel, N., Williams, J. P., & Bruderer, S. 2018, ApJL, 867, L14
van Zadelhoff, G. J., van Dishoeck, E. F., Thi, W. F., & Blake, G. A. 2001, A&A, 377, 566
van't Hoff, M. L. R., Tobin, J. J., Trapman, L., et al. 2018, ApJL, 864, L23
Villenave, M., Ménard, F., Dent, W. R. F., et al. 2020, A&A, 642, A164
Wakelam, V., Chapillon, E., Dutrey, A., et al. 2019, MNRAS, 484, 1563
Walsh, C., Loomis, R. A., Öberg, K. I., et al. 2016, ApJL, 823, L10
Walsh, C., Millar, T. J., Nomura, H., et al. 2014, A&A, 563, A33
Yen, H.-W., Koch, P. M., Liu, H. B., et al. 2016, ApJ, 832, 204
Zhang, K., Booth, A. S., Law, C. J., et al. 2021, ApJS, 257, 5